Doctoral Dissertation

Study on Electrical Analysis of Single-Particles and -Molecules Using Extended-Nanospace in Aqueous Conditions

February 2016

Akihide Arima

Study on Electrical Analysis of Single-Particles and -Molecules Using Extended-Nanospace in Aqueous Conditions

Contents

Chapter 1 General introduction

In his famous lecture "There's Plenty of Room at the Bottom" at annual meeting of American Physical Society (1959), American physicist Richard Phillips Feynman predicted the rise of nanotechnology[1]. After a half century later, the progress in science and technology opened the gate of nanoscience and enabled to address various novel phenomena mostly related to quantum physics due in part to the intense motivation to pursue Moore's law in semiconductor industries that aimed to miniaturize field effect transistors in integrated circuits[2-4]. Nowadays, these knowledge and techniques have been spread to other field including bioscience and biotechnology[5-6].

One of the growing field utilizing these advantages is single-molecule electronics. In 1974, American materials chemist, Ari Aviram and Mark A. Ratner, propounded theoretical feasibility of molecular electronics[7]. After several decades, an exciting achievement was made by Mark A. Reed who applied a break junction method to realize conductance measurements of single-molecules connected to two metal electrodes[8]. Together with the progress in nanotechnology, this important milestone contributed greatly to make single-molecule measurements more feasible in laboratory tests and led to recent applications of single-molecule techniques not only for developing single-molecule building blocks for future nanoelectronics but also for bioanalytical applications that promises single-molecule resolution[9-14]. As the representative of former field, the research of thermoelectric conversion has been progressed on the view of single molecule region where various materials shows different property with bulk form[9-11]. These research are expected to achieve green technology by direct conversion of heat into electrical energy with high-efficiency. On the other hand, in latter field, researchers take full advantage of nanotechnology to develop single-molecule techniques useful for

achieving high-throughput single-molecule analysis of bio-particles and –molecules[12-14].

Structural proteomics is one of the field where single-molecule techniques are expected to play an important role as a method to analyze structure of individual proteins thereby replacing the present analytical methods which provide information of analyte as an average of bulk form. Considering the record of the past, there are plenty of potential methods to acquire information about structure of biomolecules. For instance, X-ray crystallography is a prolific method to obtain structural information of miscellaneous materials including biomolecules, and is widely applied in determining structure of

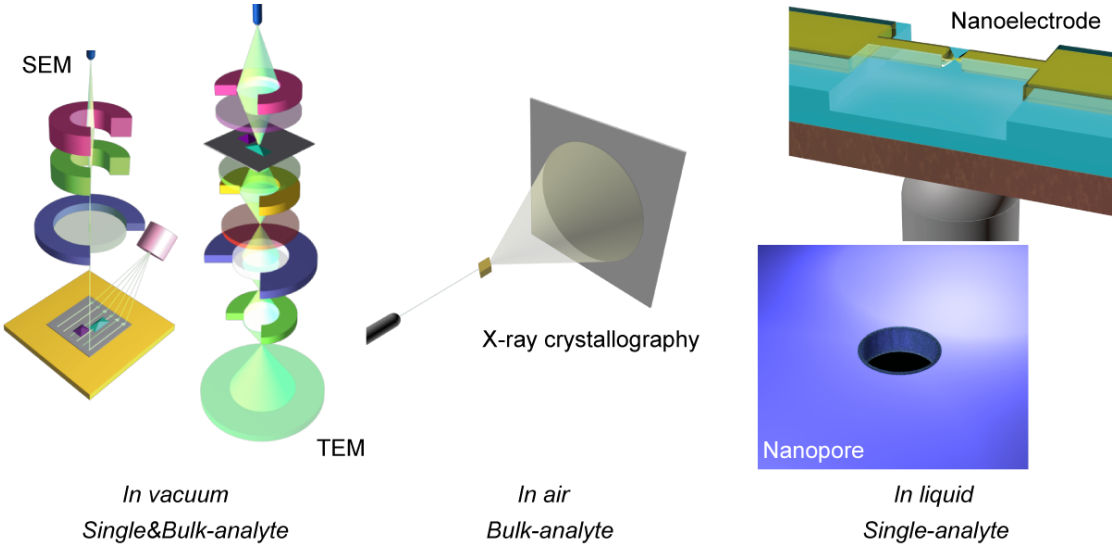

Figure 1. Various method for bioanalysis in micro-nano region.

proteins at atomic-scale[15-16]. However, this method has disadvantage in the critical difficulty of making large yet high-quality single crystal samples. Also, it only provides averaged molecular structure and cannot be used to address the structure of single-molecules in liquid media where the biomolecules demonstrate the fascinating biofunctionality. On the other hand, scanning probe microscopy can give atomic-scale images of isolated single-molecules fixed on a flat substrate[17-18]. In particular, in-situ atomic force microscopy (AFM) and STM is proven useful in visualizing proteins in

liquid[19-20]. However, these methods has disadvantage in efficiency because of necessity to seek target molecules.

As described above, tradition and innovation of science and technology shed light on the micro- to nano-scale world. However, it is still a formidable task to achieve to investigate single-molecule structure and its dynamic motions in a liquid. Although time resolution of fluorescent microscope techniques has been improved to enable live cell imaging, the achievement of which led to novel prize in 2014[21-23], the spatial resolution is in principle limited to sub-micrometer scale by the wavelength of the light. Meanwhile, nanopores and nanoelectrodes have recently been employed as a useful platform to identify individual molecules and particles at nanoscale. Nanopore is a nanoscale hole formed in a thin membrane, which can be either a bilayer lipid or solid thin film suspended on a substrate[24-27]. The method involves measurements of the ionic current in the pore channel filled with an electrolyte solution under the condition of electrophoresis[28]. The ion flow is blocked when a particle or a molecule passes through there, which can be detected as a temporal drop in the ionic current. As larger analytes will exclude more ions, one can estimate the size of the objects from the current signatures. Nanoelectrodes are, on the other hand, employed to measure the tunneling current flowing through a pair of electrodes immersed in a liquid[29-30]. Molecules trapped in the electrode gap carries current conducted via the molecular orbitals that electronically couple with the electrodes, thereby giving a current rise in the current-time trace. As the tunneling current reflects the molecular orbital levels unique to the molecules, it can be utilized as a useful parameter to identify single-molecules.

One of the important applications of these two methods to single-molecule scale is DNA sequencing via tunneling current based on the ionic current blockades and the

tunneling current[31-32]. To acquire basic knowledge for nanopore sequencing, much effort has been devoted to test a low-thickness-to-diameter aspect ratio pore with ultra-thin thickness to achieve single-base resolution required to read-out any genome sequence. As the spacing between nucleobases in DNA and RNA is about 0.3 nm, atomic-sheet materials such as graphene and boron nitride have been used as a membrane to enhance the spatial resolution up to sub-nanometer level[33-34]. Beside, in recent years, several groups applied the low-aspect-ratio pores to the analysis of local structural change in nanopore itself and also for discrimination of protein forms in a liquid[35-37]. In addition, nanopores are found in recent studies to serve as a trap field to capture and immobilize single-analyte at a predefined positions at nanoscale through controlling the electrophoresis by modulation of the diameter of a pore[38]. Combining the means to control the analyte dynamics via this nanopore trapping method to the tunneling current approach can be a promising way to improve the discriminability of single-nucleotides, which requires a nanosensor consisting of a pair of nanoelectrodes embedded in a nanopore.

Here, in this thesis, a method to address structure and dynamic motions of single-biomolecules and –particles in a liquid using nanopores and nanoelectrodes via the evaluation of conductivity. In nanopore sensing, analyte discriminations via the surface charge status were demonstrated through the ionic current measurements in a low-aspect-ratio pore, wherein it was found that the counterions on analyte particles brings additional ions in the channel during translocation thereby contributing to enhance the cross-pore current as opposed to the volume exclusion effects. The low-aspect-ratio nanopores were also utilized as a tool to trap an oversized analyte so as to verify the effectiveness to trap and immobilize single-molecules in an extended-nanospace for the envisaged tunneling

current measurements via electrode-embedded nanopores. For this, a microfluidic channel integrated nanopore device was fabricated to perform simultaneous measurements of fluorescence and the cross-pore ionic current for studying the dynamic motions of particles before and after trapping at the pore. The optical observations elucidated little fluctuations in the particle motions after being trapped due to the strong electrophoretic forces derived from the huge electric field at the pore that overwhelms the kinetic energy of the water molecules at ambient conditions typified by Brownian motion. To incorporate the method to the tunneling current measurements, a nanopore, or a nanowell, was integrated to a microfabricated mechanically-controllable break junction. In this device, a back electrode formed at the bottom of the well can be used for imposing an electric field to capture analytes while the break junction technique forms a molecular-sized electrode gap inside there for single-molecule detections by tunneling current. Here, a special care was taken to suppress the ionic current through the nanoelectrodes that deteriorates the single-molecule sensing capability by adding more noise on the current. The idea was to cover the entire surface of the nanoelectrodes except nanoscale apex used to measure the tunneling current. Although this cannot be easily accomplished by nanolithography processes alone, it was found that breaking SiO_2-covered metal junctions can give such structure. Besides, the nanoelectrodes were applied for discrimination of single-proteins and their dynamic motions in buffer solution at room temperatures via the ionic and tunneling current. This study gives better fundamental understanding of the electron transport through single-biomolecules useful for structural analysis of protein molecules.

Reference of general introduction

1. R. P. Feynman, *Engineering and Science* **23**, 5 (1960).
2. H. Song, Y. Kim, Y. H. Jang, H. Jeong, M. A. Reed, and T. Lee, *Nature* **462**, 1039 (2009)
3. D. Dulić, S. J. van der Molen, T. Kudernac, H. T. Jonkman, J. J. D. de Jong, T. N. Bowden, J. van Esch, B. L. Feringa, and B. J. van Wees, *Phys. Rev. Lett.* **91**, 207402 (2003)
4. P. Reddy, S.-Y. Jang, R. A. Segalman, A. Majumdar, *Science* **315**, 1568 (2007)
5. A. Manz, N. Graber and H. Widmer, *Sensors and Actuators B : Chemical* **1**, 244 (1990)
6. D. Matsumoto, R. R. Sathuluri, Y. Kato, Y. R. Silberberg, R. Kawamura, F. Iwata, T. Kobayashi, and C. Nakamura, *Sci. Rep.* **5**, 15325 (2015)
7. A. Aviram and M. A. Ratner, *Chem. Phys. Lett.* **29**, 277 (1974).
8. M. A. Reed, C. Zhou, C. J. Muller, T. P. Burgin, J. M. Tour, *Science* **278**, 252 (1997)
9. M. Tsutsui, T. Morikawa, A. Arima, M. Taniguchi, *Sci. Rep.* **3**, 3326 (2013)
10. T. Morikawa, A. Arima, M. Tsutsui, M. Taniguchi, *Nanoscale* **6**, 8235 (2014)
11. M. Tsutsui, T. Morikawa, Y. He, A. Arima, and M. Taniguchi, *Sci. Rep*. **5**, 11519 (2015)
12. D. Branton, D. Deamer, A. Marziali, H. Bayley, S. Benner, T. Butler, M. Ventra, S. Garaj, A. Hibbs, X. Huang, S. Jovanovich, P. Krstic, S. Lindsay, X. Ling, C. Mastrangelo, A. Meller, J. Oliver, Y. Pershin, J. Ramsey, R. Riehn, G. Soni, V. Tabard-Cossa, M. Wanunu, M. Wiggin, and J. Schloss, *Nat. biotechnol.* **26**, 1146 (2008)
13. M. Wanunu, J. Sutin, B. McNally, A. Chow, A. Meller, *Biophys. J.* **95**, 4716 (2008).

14. D. S. Talaga, J. Li, *J. Am. Chem. Soc.* **131**, 9287 (2009)
15. J. C. Kendrew, G. Bodo, H. M. Dintzis, R. G. Parrish, H. Wyckoff, and D. C. Phillips, *Nature* **181**, 662 (1958)
16. J. Deisenhofer, O. Epp, K. Miki, R. Huber, H. Michel, *J. Mol. Biol.* **180**, 385 (1984)
17. J. Morimoto, H. Tanaka, T. Kawai, *Sur. Sci.* **580**, L103 (2005)
18. G. B. Khomutov, L. V. Belovolova, V. V. Khanin, E. S. Soldatov, A. S. Trifonov, *Colloids Surf. A* **198**, 745 (2002)
19. S. Ido, H. Kimiya, K. Kobayashi, H. Kominami, K. Matsushige, and Y. Yamada, *Nat. Mater.* **13**, 264 (2014)
20. Q. Chi, O. Farver, J. Ulstrup, *Proc. Natl. Acad. Sci. USA* **102**, 16203 (2005)
21. E. Betzig, G. H. Patterson, R. Sougrat, O. W. Lindwasser, S. Olenych, J. S. Bonifacino, M. W. Davidson, J. Lippincott-Schwartz, H. F. Hess, *Science* **313**, 1642 (2006)
22. T. A. Klar, S. Jakobs, M. Dyba, A. Egner, S. W. Hell, *Proc. Natl. Acad. Sci. USA* **97**, 8206 (2000)
23. R. M. Dickson, A. B. Cubitt, R. Y. Tsien, W. E. Moerner, *Nature* **388**, 355 (1997)
24. S. Huang, M. Romero-Ruiz, O. K. Castell, H. Bayley, and M. I. Wallance, *Nat. Nanotechnol*. **10**, 986 (2015)
25. G. Maglia, M. R. Restrepo, E. Mikhailova, H. Bayley, *Proc. Natl. Acad. Sci. USA* **105**, 19720 (2008)
26. A. J. Storm, C. Storm, J. Chen, H. Zandbergen, J.-F. Joanny, and C. Dekker, *Nano Lett.* **5**, 1193 (2005)
27. S. Garaj, W. Hubbard, A. Reina, J. Kong, D. Branton, and J. A. Golovchenko, *Nature* **469**, 190 (2010)

28. W. H. Coulter, *U.S. pat.* 2,656,508. (1953)
29. M. Tsutsui, M. Taniguchi, K. Yokota, T. Kawai, *Nat. Nanotechnol*. **5**, 286 (2010)
30. S. Huang, J. He, S. Chang, P. Zhang, F. Liang, S. Li, M. Tuchband, A. Fuhrmann, R. Ros, and S. Lindsay, *Nat. Nanotechnol*. **5**, 868 (2010)
31. M. Zwolak and M. Di Ventra, *Rev. Mod. Phys.*, **80**, 141 (2008)
32. W. Vercoutere, S. Winters-Hilt, H. Olsen, D. Deamer, D. Haussler, and M. Akeson, *Nat. biotechnol.*, **19**, 248 (2001)
33. C. A. Merchant, K. Healy, M. Wanunu, V. Ray, N. Peterman, J. Bartel, M. D. Fischbein, K. Venta, Z. Luo, A. T. C. Johnson, and M. Drndić, *Nano Lett.* **10**, 2915 (2010)
34. S. Liu, B. Lu, Q. Zhao, J. Li, T. Gao, Y. Chen, Y. Zhang, Z. Liu, Z. Fan, F. Yang, L. You, D. Yu, *Adv. Mater.* **25**, 4549 (2013)
35. C. Plesa, S. W. Kowalczyk, R. Zinsmeester, A. Y. Grosberg, Y. Rabin, and C. Dekker, *Nano Lett.* **13**, 658 (2013)
36. D. J. Niedzwiecki, C. J. Lanci, G. Shemer, P. S. Cheng, J. G. Saven, and M. Drndic, *ACS Nano* **9**, 8907 (2015)
37. J. Larkin, R. Y. Henley, M. Muthukumer, J. K. Rosenstein, and M. Wanunu, *Biophys. J.* **106**, 696 (2014)
38. M. Tsutsui, Y. Maeda, Y. He, S. Hongo, S. Ryuzaki, S. Kawano, T. Kawai, and M. Taniguchi, *Appl. Phys. Lett.* **103**, 013108 (2013)

Chapter 2 Single-particle analysis using a low thickness-to-diameter aspect ratio nanopore

Introduction

Nanopore devices are applied in various field as an excellent sensor for non-destructive analysis of biological particles and molecules.[1-6] The measurement principal is simple; in salt solution containing analyte, electric field is applied on a pore in a thin membrane. Under the field, charged objects are moved electrophoretically. When an analyte reaches and passes through the pore channel, their volume excludes ions inside the pore. One can observe this volume exclusion effect as a sudden drop of the ionic current through the pore in forms of spike signals that contains information of volume of individual analytes. This method is invented by Wallace H. Coulter and has been adopted explosively in especially biological field.[7] Recent progress of nanotechnology has made it recapture the spotlight for analysis in single molecular scale.

Recently, in the field of nanopore analysis, a low thickness-to-diameter aspect ratio nanopore received great attention because of its envisaged higher spatial resolution.[8] In case of a high aspect ratio nanopore, an analyte is completely stored in the conduit during translocation. This enables the aforementioned particle size assessments. On the other hand, the excluded volume inside the pore can be made smaller by employing a low aspect ratio nanopore structure. Then, when a particle passes through the thin pore, the volume exclusion effects would be expected to give rise a change in the cross-pore ionic current that reflects the fine shape, instead of the whole volume, thereby allowing single-particle shape analysis

Previous studies have in fact demonstrated single-particle detections using low-aspect ratio nanopores. Several groups used an atomic layer formed by a bottom-up

approach such as CVD-grown graphene[8], boron nitride[9], and MoS[10] as an ultrathin membrane for realizing a nanopore sensor with sub-nanometer level spatial resolution to discriminate the size difference of single nucleotides of DNA. In these works, the ultra-thin nanopores were proven useful in detecting single-molecules though the excessively fast translocation speed of DNA under the electrophoretic voltage posed a challenge to accomplish single-molecule sequencing.

Although promising, however, the sensing mechanism of the low aspect ratio pore sensors is still not established due to the increasing roles of the resistance outside the pore, which is called access resistance.[11] From theoretical viewpoint, the cross-pore ionic current becomes sensitive to a change in the access resistance as lowering the pore aspect ratio due to the relative importance of the resistance at the exterior regions of the pore compared to the interior counterpart. This indicates that the ionic current tends to be affected appreciably in prior to particle translocation as occupation of the pore orifice by the particle would alter the ion conductivity through the pore, which in turn indicates that one cannot attain high spatial resolution by simply lowering the pore thickness. Several groups have attempted to shed light on the factors that would determine the ionic current blockades in a low aspect ratio pore. Tsutsui et al.[12] utilized an ultrathin micropore in a SiN membrane for single-nanoparticle detections and demonstrated that the ionic current signal height scales with the analyte volume. In their study, it was also observed that the access resistance remained unchanged during the particle translocation despite that they occupied the pore orifice in prior to translocation. This intriguing results were reproduced by Davenport et al.[13] where the authors systematically evaluated the dependence of the ionic current spike height on the pore aspect ratio structure and found invariable access resistance in a nanopore having the thickness-to-diameter aspect ratio lower than a certain

value. These studies somehow suggested that, in contrary to the theoretical anticipation, a high spatial resolution can be accomplished in a low aspect ratio nanopore.

In this chapter, the capability of a low aspect ratio nanopore is investigated in an effort to assess the prospect for structural analysis of single-biomolecules by unveiling the mechanism underlying the peculiar observation of constant access resistance during particle translocation. It begins with an introduction explaining the principle of nanopore analysis with an emphasis on the role of access resistance (2.1). After that, experimental results of ionic current blockage by equi-sized nanoparticles with different surface charge status in a low aspect ratio micropore are shown (2.2), wherein it was found that the counterions on the particle surface would affect the cross-pore ionic current giving rise to the virtually invariable access resistance during the translocation. As this finding indicated a difficulty in accomplishing particle shape analysis by simply employing a low aspect ratio pore, an alternative means for single-biomolecule analysis was pursued where a nanopore was exploited as a tool to trap a nanoscale object at the pore orifice (2.3). In the study, the mechanism responsible for electrophoretic trapping of single-particles at a low aspect ratio pore is explored by fabricating a microfluidic channel integrated micropore device and using it for simultaneous monitoring of the cross-pore ionic current and fluorescence of dyed polymer microbeads. It was revealed that the nanopore trapping method can be used to trap and immobilize particles at the pore. As will be described in Chapter 4, the nanopore trapping mechanism is applied for single-particle detections via transverse ionic current in electrode-embedded pore sensors.

Reference of introduction

1. H. Bayley and C. R. Martin, *Chem. Rev.* **100**, 2575 (2000)
2. Z. D. Harms, D. G. Haywood, A. R. Kneller, L. Selzer, A. Zlotnick and S. C. Jacobson, *Anal. Chem*. **87**, 699 (2015)
3. J. D. Uram, K. Ke, A. J. Hunt and M. Mayer, *Small* **2**, 967(2006)
4. N. Arjmandi, W. Van Roy, L. Lagae and G. Borghs, *Anal. Chem.* **84**, 8490 (2012)
5. C. Plesa, S. W. Kowalczyk, R. Zinsmeester, A. Y. Grosberg, Y. Rabin and C. Dekker, *Nano Lett*. **13**, 65 (2013)
6. S. Howorka and Z. S. Siwy, *Nat. Biotechnol*. **30**, 506 (2012)
7. W. H. Coulter, *US Pat.* 2,656,508 (1953)
8. C. A. Merchant, K. Healy, M. Wanunu, V. Ray, N. Peterman, J. Bartel, M. D. Fischbein, K. Venta, Z. Luo, A. T. C. Johnson and M. Drndić, *Nano Lett.* **10**, 2915 (2010)
9. Z. Zhou, Y. Hu, H. Wang, Z. Xu, W. Wang, X. Bai, X. Shan, and X. Lu, *Sci. Rep.* **3**, 3287 (2013)
10. K. Liu, J. Feng, A. Kis, and A. Radenovic, *ACS Nano* **8**, 2504 (2014)
11. J. Wang, J. Ma, Z. Ni, L. Zhang, and G. Hu, *RSC Adv.* **4** 7601 (2014)
12. M. Tsutsui, S. Hongo, Y. He, M. Taniguchi, N. Gemma, and K. Tomoji, *ACS Nano* **6**, 3499 (2012).
13. M. Davenport, K. Healy, M. Pevarnik, N. Teslich, S. Cabrini, A. P. Morrison, Z. S. Siwy, and S. E. Létant, *ACS Nano* **6**, 8366 (2012).

2.1. Nanopore measurement

A nanopore measurement uses electrophoresis to propel analytes into the channel for detections[1-2]. The driving forces relevant for the nanopore analysis are thus categorized into three factors: the electrophoretic force, the drag force of an electroosmotic flow in the pore, and the hydrodynamic force under pressure[3]. In aqueous conditions, the charged objects feel the electric field and move electrophoretically under the electrostatic forces. Alike the analytes, the pore wall becomes also charged when immersed in aqueous conditions. The surface charges are screened by other ions and electric double layer is formed on the wall. In experiment, the electrophoretic voltage effectively moves these counterions, and therefore produces a flow of water in vicinity of the wall surface. In large scale experiment, the effect of electroosmotic flow is not so important. However, as scale down of the system, this follow shows presence. For example, in capillary electrophoresis, this electroosomosis often determines the flow direction and speed of analytes due to that the electrophoretic forces are weaker than the electroosmotic dragging. As described above, the electroosmotic flow becomes even more important in considering the electrokinetics of analyte translocation as they will be forced to pass through a nanometer-vicinity of the pore wall surface whereat the electroosmotic flow is strongest.

Theoretically, the nanopore measurement system is expressed by the following series resistance model[4],

$$R = R_{\text{pore}} + 2R_{\text{acc}}$$

, where R_{pore} is the pore resistance and R_{acc} is the so-called access resistance, which is the resistance from the electrode at infinity distance to the pore orifice. Each resistance is

described by the following equations.

$$R_{pore} = 4\rho L/\pi d^2$$

$$R_{acc} = \rho/2d$$

Here, ρ, L, and d are the solution resistivity, the membrane thickness, and the diameter of a pore, respectively. For a low aspect ratio nanopore, L becomes smaller and pore resistance decreases to almost 0; as a result, the access resistance becomes predominant and tends to determine the total resistance. This theoretical expression was found useful in understanding open pore ion transport. Garaj et al.[5] reported linear increase in the graphene nanopore conductance with the pore diameter in a low aspect ratio regime that showed excellent agreement with the theoretical expectation. Dekker et al.[6] further built a sophisticated model that even took into account the fine structure of the pore, for instance hourglass or tapered shapes.

On the other hand, as mentioned in 2.1, the resistance change of low aspect ratio pores during particle translocation is far from comprehensible where it was experimentally observed that R_{acc} changes little upon a particle passing through the pore. In fact, beyond the above simple analytical model, recent finite element analyses suggested increasing influence of counterions on the particle surface as well as those on pore wall that basically tends to enhance the cross-pore ionic current by providing more ions into the pore during their translocation. Therefore, although low aspect ratio pores have been considered as promising for analyzing nanoscale shapes of analytes, it is crucial to have better fundamental understanding of ion transport characteristics in such pores to seek for any applications.

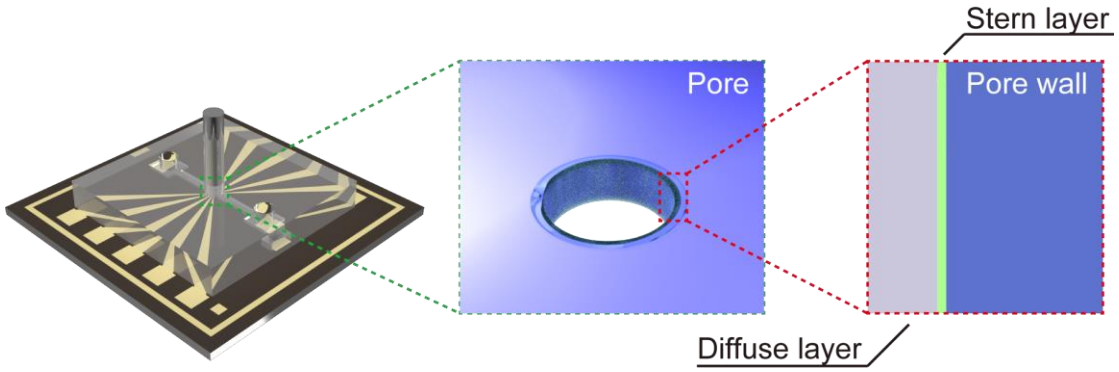

Figure 2.1. The magnified image of nanopore device.

Reference of this section

1. W. H. Coulter, *US Pat.* 2,656,508 (1953)
2. J. E. Hall, *J. Gen. Physiol.* **66**, 531(1975)
3. M. Davenport, K. Kealy, M. Pevarnik, N. Teslich, S. Cabrini, A. P. Morrison, Z. S. Siwy, and S. E. Létant, *ACS Nano* **6**, 8366 (2012)
4. M. Tsutsui, S. Hongo, Y. He, M. Taniguchi, and T. Kawai, *ACS Nano* **6**, 3499 (2012)
5. S. Garaj, W. Hubbard, A. Reina, J. Kong, D. Branton, and J. A. Golovchenko, *Nature* **469**, 190 (2010)
6. S. W. Kowalczyk, A. Y. Grosberg, Y. Rabin, and C. Dekker, *Nanotechnology* **22**, 315101 (2011)

2.2. Discrimination of surface charge density of analyte using a low-aspect-ratio nanopore

For approaching encompassing information of analytes, form and surface are main factors. Besides, in these days, various problems concerning micro- and nano-scale objects such as particulate matter (PM) 2.5 and 10 are stepping up their presence because of its harmful effect to human health[1-2]. However, high-throughput method to characterize the health risk of these objects has not been established yet. One of the possible way for fulfilling these demands is to use the single-particle sensing ability of micro- and nanopore devices as particle analyzers[3-5].

To achieve this challenge, however, it is of crucial importance to distinguish them not only by the sizes as done in Coulter counter but also by the agreeability and sorbability that determine their risk on serious diseases such as cancer.[6] Generally, however, nanopore sensors are essentially applicable for discerning particles by their volume and the possible influence of the particle's surface charges are seldom considered in the particle analysis.

Therefore, in this section, it was verified to discriminate particles not by the size but by the surface charge density by the theoretically predicted high sensitivity of the ionic current blockade effects on the particles' counterions in a low aspect ratio sensor. For this, solid-state low-aspect ratio (< 0.08) nanopores were used to detect single-nanoparticles of the same size but having functionalized by different groups such as COOH, NH_2, OH, and SO_2 by the ionic current measurements. These knowledge might be helpful in pattern analysis for the bioparticles such as proteins.

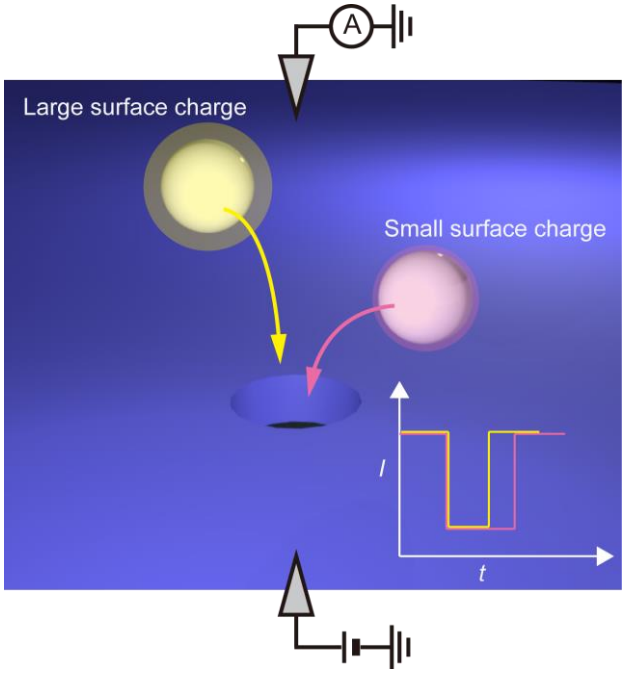

Figure. 2.2.1. Discrimination of equi-sized nanoparticles.

Figures 2.2.1 to 2.2.2 are reproduced from *Appl. Phys. Lett.* 104, 163112 (2014) with the permission of AIP publishing

2.2.1. Fabrication of low thickness-to-diameter aspect ratio nanopore devices

A 4 inch silicon wafer constructed with three layers, SiN/Si/SiN = 50 nm/0.5 mm/50 nm, was used as a substrate. This wafer was cut to 20 mm × 20 mm size chips and positive type photoresist TSMR V50 was spin-coated on one side of the surface. The resist layer was removed partially using a photolithography method and the exposed SiN layer was etched by reactive ion etching (RIE). Then, a few centimeters-long Teflon tube was connected to this area and potassium hydroxide aqueous solution was poured into the tube to dissolve the Si layer by (111) anisotropic etching. In this process, the substrate was placed on a hot plate and heated to 120 degrees Celsius for expediting the etching. Eventually, the etching was stopped by the SiN layer at the other side as it has high resistance to the wet etching. As a result, a 50 nm-thick SiN membrane was formed. Subsequently, the metal makers (thickness: Cr/Au/Cr = 2 nm/30 nm/2 nm) for electron-beam lithography was deposited by a photolithography process followed by Cr/Au deposition by radio-frequency magnetron sputtering and lift-off in *N*, *N*-dimethylformamide (DMF). Then, electron-beam (EB) resist ZEP-520A was spin-coated and 0.7 or 1.0 μm-sized pore was drawn by scanning electron beam on the membrane. The pore was drilled by RIE using the EB resist as a mask. Finally, residual resist was removed by immersing the substrate in DMF overnight.

For the introduction of sample solutions, polydimethylsiloxane (PDMS) blocks, which had a microtrench on one side of the surface, were attached on both sides of the pore chips by hydrophilic treatment using oxygen plasma etching.[7] After the induction, Ag/AgCl electrodes were set on the both sides. Dry cell battery was used to apply the electrophoretic voltage and high-speed current amplifier (AXIS NET INC.) and PCI

eXtensions for Instrumentation (National Instruments) under the control of handmade LabVIEW program was utilized measure the ionic current flowing through the Ag/AgCl electrodes via the pore.

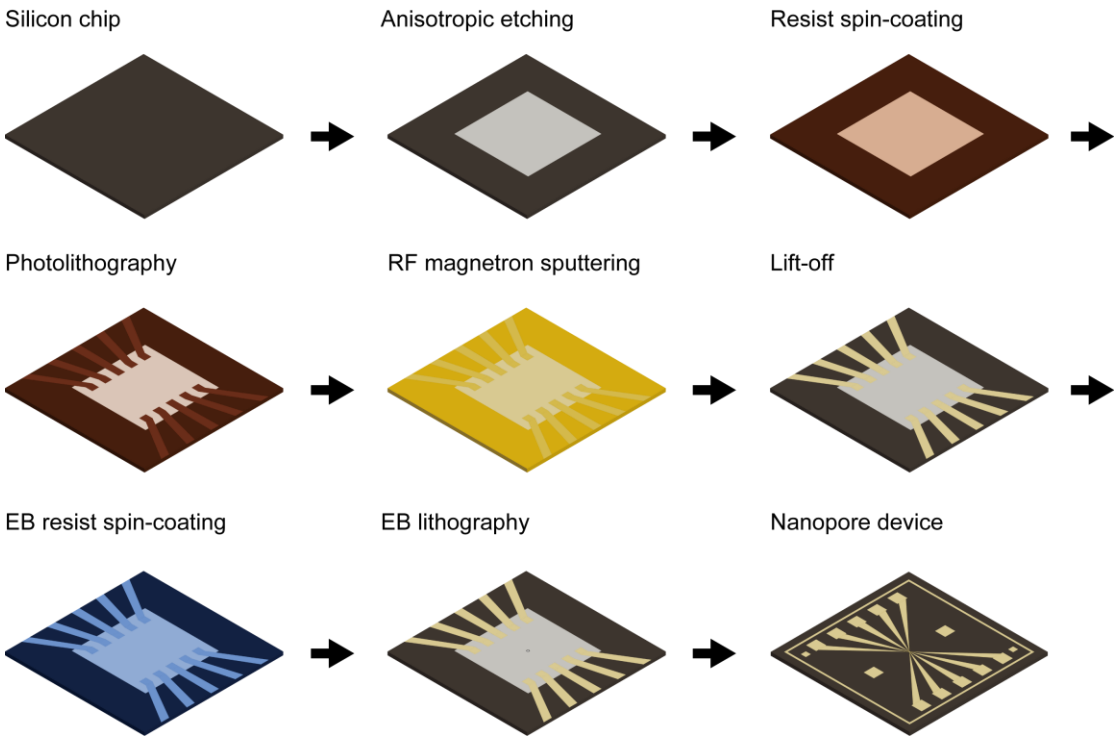

Figure. 2.2.2. Fabrication process of nanopore device.

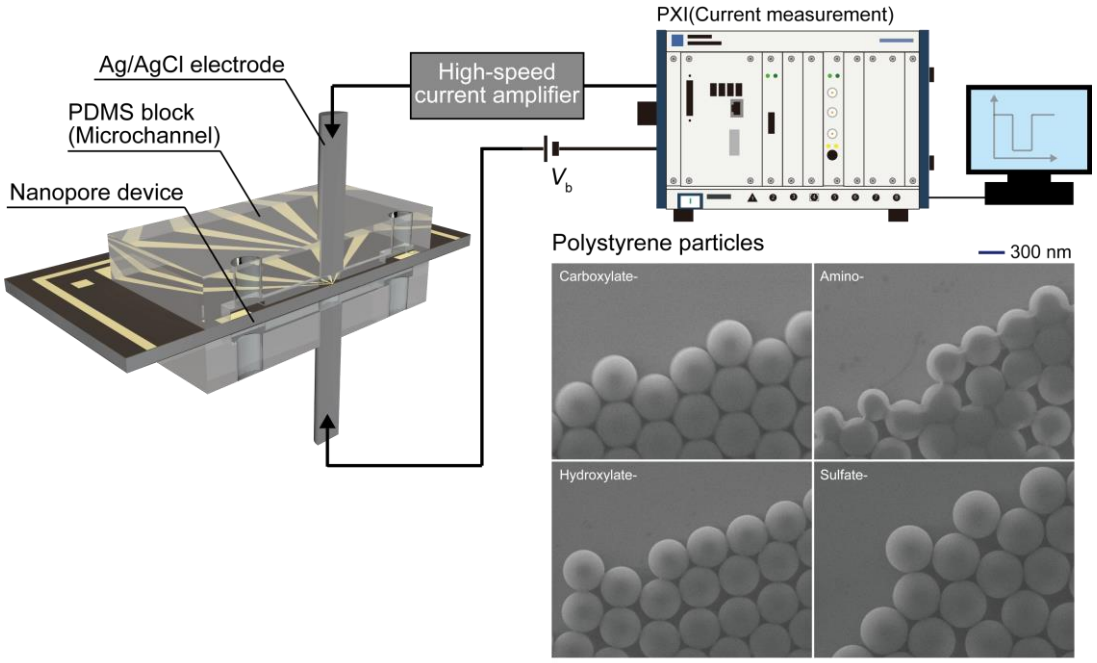

Figure. 2.2.3. Setup of small current measurement using nanopore device and polystyrene particles

2.2.2. Ionic current measurement using nanopore devices

Cross-sectional images of the pore device are shown in Figure 2.2.3. As described in the above section, this device is constructed with a silicon chip with a nanopore in the 50 nm thick SiN membrane sealed by the PDMS blocks having microchannels for induction of sample solutions on the both sides. The aspect ratios of 0.7 and 1.0 μm-sized pores are approximately 0.07 and 0.05, respectively. Scanning electron micrographs (SEM; HITACHI S-4300) of polystyrene nanoparticles utilized as target analyte are also shown in this Figure. Each particle is 500 nm-sized but chemically modified with different functional groups (carboxylate-, amino-, hydroxylate-, and sulfate-). In these images, clear shape of sphere are conformed, though the difference of surface charge density cannot be distinguished. These particles are dispersed in TE buffer (Tris-HCl 10 mM, EDTA 1 mM) at a concentration of 25 ng/μL. The sample solution containing target particles was injected into one side of the PDMS channels and the other side was filled with the buffer only. The bias voltage sign was set to electrophoretically flow the negatively-charged target particles into a pore.

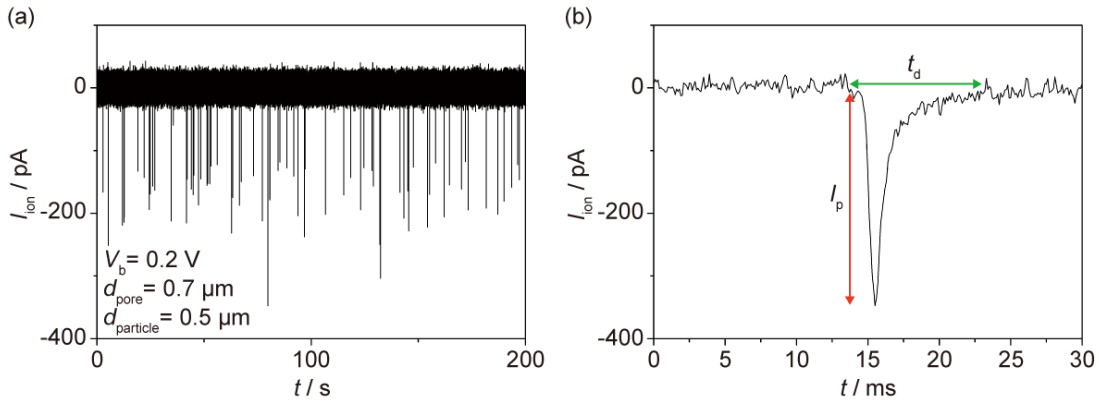

Figure 2.2.4. (a) Typical I_{ion}-t curve showing resistive pulses. (b) Magnified view of an ionic spike characterized by the height I_p and width t_d.

The representative current signals are shown in Figs. 2.2.4(a) and (b).[8-9] Current spikes are observed characterized by I_p and t_d, which denote the amplitude and the width of the current spikes, respectively. The spike forms are found similar for the four kinds of target polystyrene particles used that are functionalized with either carboxylate, amine, hydroxylate, or sulfate. The value of I_p mainly reflects the temporal blocking of the transport of ions by volume of particles and t_d is attributed to the time required for the particles to electrophoretically move through the pore.

The histograms of each value are constructed to statistically analyze the influence of the surface charge status on the ionic conductance (Figure 2.2.5.). The peak values of I_p and t_d extracted by Gaussian fitting to each distribution are adopted as representative characteristics of each modified particle; I_{ppst} and t_{dpst}. In the I_p histograms, a bimodal distribution are observed for the 1.0 μm pore and only monomodal ones except the sulfate particles in the 0.7 μm pore. On the other hand, histograms of the dwell time revealed only one peak. Apart from the surface charge effects, the resistance with a particle residing in the low aspect ratio pore can be expressed by the following equation[10]

$$R = 4\rho L/\pi\,(d_{pore}^2 - d_{particle}^2) + \rho/d_{pore}$$

under the assumption of constant R_{acc}, where ρ denote the conductivity of TE buffer 12.7 Ωm and d_{pore} and $d_{particle}$ are the diameters of a pore and particle, respectively.[8] The calculated values of ionic current I_{cal} are derived using the above equation. Interestingly, compared with I_{cal}, I_{ppst} is smaller for all types of particles examined. As described above, the ionic blockade signals are affected by various reasons other than volume exclusion effects. Lan and his colleagues[11] researched an effect of charged nanoparticles to the ionic current spike shapes using glass nanopores. They revealed that it stems from ion accumulation and depletion associated with charges of the particle. Furthermore, Wang

and co-workers[12] focused on this effect theoretically and indicated that the low aspect ratio nanopore is sensitive to the surface charge density of nanoparticle than the high-aspect-ratio counterparts. Therefore, the difference of I_{ppst} smaller than I_{cal} experimentally indicated that counter ions on the polystyrene particles contributed to increase the amount of current-carrying charge carriers and mitigate the pore resistance increase via volume exclusion effect upon passing through the low-aspect ratio nanopore.

Furthermore, to compare the experimental results and verify the possibility of

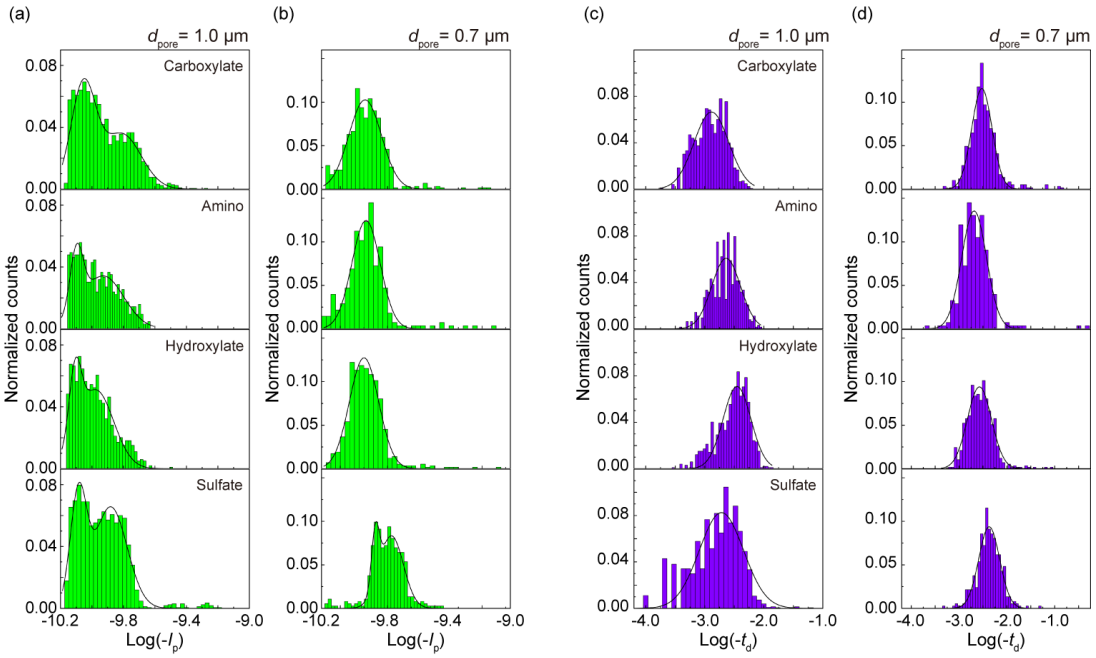

Figure 2.2.5. Statistical distribution of ionic current (green) and duration time (purple) at 1.0 μm and 0.7 μm pore about different modified polystyrene particles. Solid lines are Gaussian fits to the histograms.

discriminating the surface charge status of each particle, the relative blockade current $I_r = 100(I_{cal} - I_{ppst})$ was calculated that denotes the percentage of I_{ppst} with respect to I_{cal} (Tables I and II). It is noted that I_r for the lower value of 1.0 μm pore are similar with those for 0.7 μm pore. As the concerning report with this result, van den Hout and co-workers[13] revealed a variation of pulse height and width attributed to the various DNA

blockade events. This report presents that the diffusing of analyte at the vicinity of the pore without passing provide a small amount current decrease by affecting the access resistance compared with that in case of translocation.[13-15] Therefore, the bimodal distribution found in I_p of the 1.0 μm pore is suggested to be due to the translocation and non-translocation events, whereas only non-translocation events were occurred in the 0.7 μm pore since the stronger drag force occurred at the pore wall would disturb the entering of particles into the pore.[16,17]

In addition to the spike height, the influence of the particle charge density on the

Table I

Modification	I_{ppst} / pA	t_{dpst} / ms	$I_{r,1.0\ \mu m}$
Carboxylate	82.0, 131	1.30	54.7, 71.7
Amino	79.8, 118	2.30	59.4, 72.7
Hydroxylate	78.2, 106	3.52	63.5, 73.0
Sulfate	88.1, 154	1.92	46.7, 69.6

Table II

Modification	I_{ppst} / pA	t_{dpst} / ms	$I_{r,0.7\ \mu m}$
Carboxylate	183	2.99	77.4
Amino	187	2.06	76.8
Hydroxylate	178	2.66	77.9
Sulfate	235, 347	4.26	57.0, 70.9

Table III

Modification	ζ-potential / mV
Carboxylate	-88.6
Amino	-54.5
Hydroxylate	-75.6
Sulfate	-86.8

Table I. Average resistive pulse height and width obtained using 1.0 μm pore. The lower group at 1.0 μm pore (left) of I_r values belongs to translocation and the higher one (right) is attached to non-translocation, Table II. Average resistive pulse height and width obtained using 0.7 μm pore, and Table III. ζ-potential of the particles.

dwell time is investigated. For this, ζ-potential of each particle dispersed in TE buffer (Table III) is measured. The order of the values are found as follows: sulfate ~ carboxylate > amino > hydroxylate. In general, larger charge density on the particle surface would give stronger electrophoretic forces that leads to higher translocation speed in the nanopore, and hence shorter dwell time. This was in fact the case for the 1.0 μm pore wherein particles could enter under the comparatively weak dragging force of

electroosmosis.[15] In contrast, it is noted that the relative amplitude order is almost reverse of that of t_{dpst} at the 0.7 μm pore. This suggests that the particles were not allowed to enter the small pore due to the electroosmotic flow. What then led to the order of t_d in 0.7 μm pore is presumably that in case of such non-translocation events, heavily charged particles tend to reach closer to the orifice of the pore whereat the electrostatic and electroosmotic force balance with each other and stay there longer that gives an ionic spike with longer t_d.

In conclusion, detections of equi-sized particles possessing different surface charge states was carried out via ionic current measurement using a low-aspect ratio nanopore sensor. Marked difference in the spike waveforms, characterized here as I_p and t_d, was observed for particles with different surface modification was shown. This result elucidated the importance of not only the size but also the counterion density on the particle surface to predict the cross-pore ionic current change during the translocation. This finding suggests the necessity to consider a possible influence of surface charge status of analytes to gain structural information from the ionic current spike pattern in a low aspect ratio nanopore sensor.

Reference of this section

1. M. Kampa and M. Castanas, *Environ. Pollut.* **151**, 362 (2008).

2. F. J. Kelly, G. W. Fuller, H. A. Walton, and J. C. Fussell, *Respirology* **17**, 7 (2012).

3. W. H. Coulter, *US Pat.* 2656508 (1953)

4. H. Zhang, C. H. Chon, X. Pan and D. Li, *Microfluid. Nanofluid.* **7**, 739 (2009)

5. T. Sun and H. Morgan, *Microfluid. Nanofluid.* **8**, 423 (2010)

6. J. Jiang, G. Oberdörster, and P. Biswas, *J. Nanopart. Res.* **11**, 77 (2009)

7. S. Bhattacharya, A. Datta, J. M. Berg, and S. Gangopadhyay, *J. Microelectron. Syst.* **14**, 590 (2005).

8. M. Tsutsui, S. Hongo, Y. He, M. Taniguchi, N. Gemma, and K. Tomoji, *ACS Nano* **6**, 3499 (2012).

9. M. Davenport, K. Healy, M. Pevarnik, N. Teslich, S. Cabrini, A. P. Morrison, Z. S. Siwy, and S. E. Létant, *ACS Nano* **6**, 8366 (2012).

10. J. E. Hall, *J. Gen Physiol.* **66**, 531 (1975).

11. W.-J. Lan, C. Kubeil, J.-W. Xiong, A. Bund, and H. S. White, *J. Phys. Chem. C* **118**, 2726 (2014).

12. J. Wang, J. Ma, Z. Ni, and G. Hu, *RSC Adv.* **4**, 7601 (2014).

13. M. van den Hout, V. Krudde, X. J. A. Janssen, and N. H. Dekker, *Biophys. J.* **99**, 3840 (2010).

14. D. M. Vlassarev and J. A. Golovchenko, *Biophys. J.* **103**, 352 (2012).

15. M. Tsutsui, Y. Maeda, Y. He, S. Hongo, S. Ryuzaki, S. Kawano, T. Kawai, and M. Taniguchi, *Appl. Phys. Lett.* **103**, 013108 (2013).

16. S. van Dorp, U. F. Keyser, N. H. Dekker, C. Dekker, and S. G. Lemay, *Nat. Phys.* **5**, 347 (2009).

17. L. Bacri, A. G. Oukhaled, B. Schiedt, G. Patriarche, E. Bourhis, J. Gierak, J. Pelta, and L. Auvray, *J. Phys. Chem. B* **115**, 2890 (2011)

2.3. Volume-specific trapping of particles in nanopores

In previous sections, the ability of low aspect ratio nanopore sensors was described where analytes were forced to pass through a pore to acquire ionic current spikes. Meanwhile, it was observed that particles were not able to enter a pore when the diameter is relatively small and electroosmotic flow is in opposite direction as that of the analyte electrophoresis. In terms of resistive pulse sensing, these non-translocation and/or clogging events are thought as "unfortunate" ones.[1] From the other point of view, however, the ionic signatures can be considered as useful in knowing whether analyte particles have been trapped at nanopores.[2]

To increase the rate the analytes go to sensing area is crucially important for effective sensing for a low-concentration sample. Recently, various ways of capturing were invented by many groups. For instance, Belkin and his colleagues[3] reported that in the system of a solid state nanopore with plasmonic nano-antennas, their molecular dynamics simulation demonstrated the possibility of direct optical trapping and controlling of displacement of DNA.

In nanopore measurements, the possibility of analyte detection relies on the chance to have those analyte particles diffusing in liquid via Brownian motions to come close enough to the pore orifice for drawing them electrophoretically in the nanopores.[4] Once drawn into a nanopore, meanwhile, the translocation speed is usually quite high so that it makes difficult to extract enough information from the short ionic current signals. On the other hand, the nanopore trapping techniques have advantages in that an individual particle can be trapped and analyzed with enough time as long as one keeps the trapping field there to clog a pore with the particle. Besides, the trapping method enables

incorporation of additional probes other than the cross-pore ionic current, such as light and tunneling current via nanoelectrode to gain wealth of information about the trapped particle.

Here, in this section, from a perspective of single-bioparticle analysis, the trapping of polystyrene beads is conducted using a low-aspect-ratio nanopore. In the experiment, we performed discrimination of particle diameter via the surface charge density. This finding can open the prospect for tracing target condition via the ionic current such as cell growth.

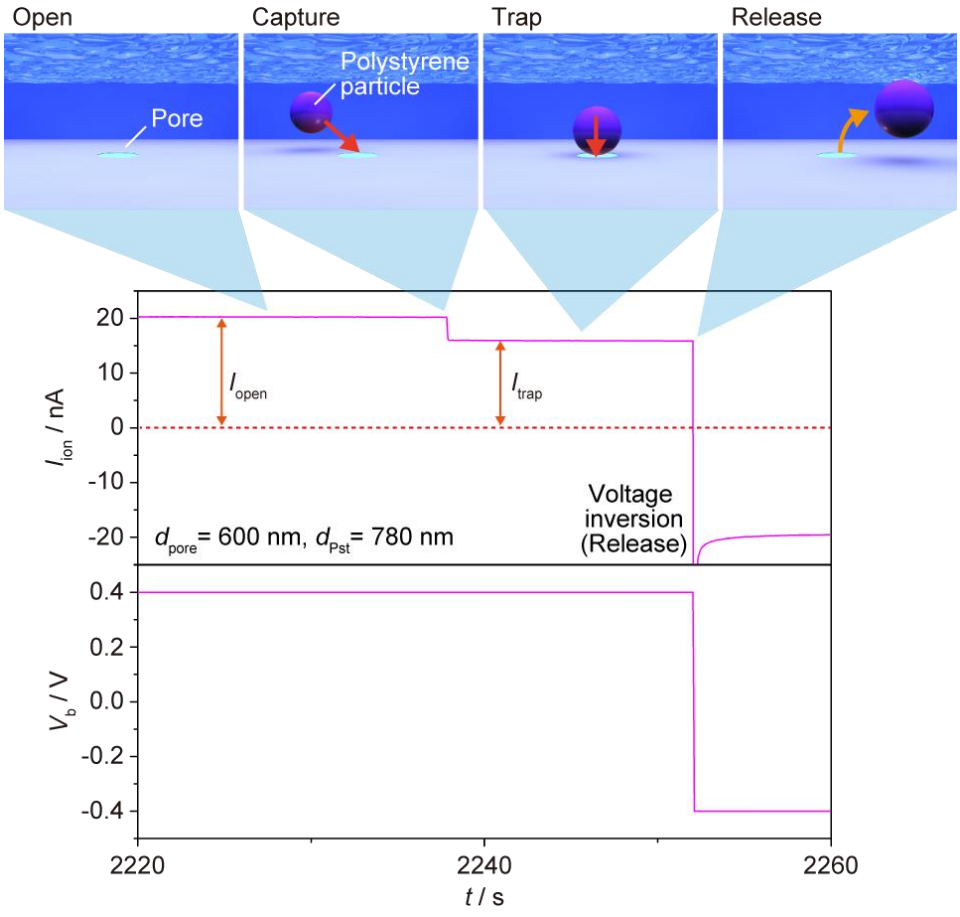

Figure. 2.3.1. The concept of nanopore trapping method.

2.3.1. The principle of nanopore trapping method and identification of particle-diameter

The principle of nanopore trapping method is based on a physical blocking of ion transport through a pore channel. In this method, a nanopore is fabricated with the diameter smaller than that of target analytes so that they cannot pass the pore but instead being clogged there. This intentional clogging can be utilized as a simple way of particle trapping at a predefined nanoscale region. Meanwhile, the presence or absence of the particles at the pore can be checked by monitoring the cross-pore ionic current: when particles are captured, the current rapidly decreases due to the partial blocking of the ion transport through the pore.

The fabrication process of nanopore is the same as that described in section 2.2.1. In this work, the diameter of a pore was set to 600 nm. On the other hand, the depth of the pore, which is defined by the thickness of the membrane used, was 50 nm. In this low aspect ratio structure, the electrophoretic voltage induces stronger electric field outside the pore due to the increasing importance of the resistance at the exterior regions of the pore compared to that inside the pore. As a result, it is expected that more particles will tend to be captured electrophoretically as the extensive electric field can effectively draw particles relatively far away from the pore. In measurements, two carboxylated-polystyrene particles with diameter 780 nm and 900 nm are utilized as target analyte. The modified region by the single carboxyl group are 51 Å and 19 Å, respectively. This means the latter particle is modified thickly; it has large surface charge density. Besides, these oversized particles are not capable of translocating through the 600 nm pore. The measurement setup, target microbeads, and nanopore utilized are shown in Figure 2.3.2. The measurement process was regulated by using a Visual Basic 6.0 program in PC

connected to Keithley 6487 picoammeter/source for applying voltage and recording small current.

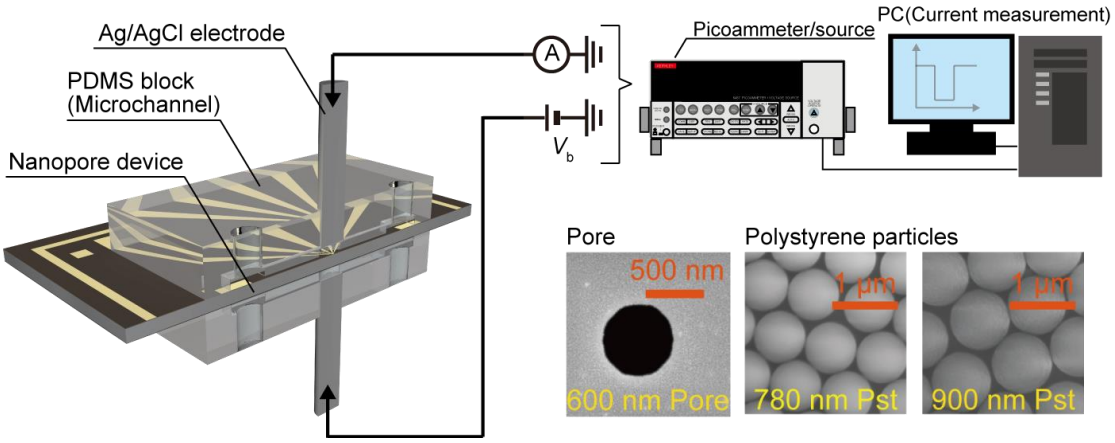

Figure 2.3.2. Setup of nanopore trapping measurement, nanopore and target microbeads.

Typical ionic current versus time trace during nanopore trapping is shown in Figure 2.3.1. Before trapping, the pore is fully open and give a constant ionic current I_{open} that scales with the pore diameter (as R_{acc} is much larger than R_{pore}). When a particle is trapped, the flow of ions is blocked and the current suddenly drops to I_{trap}. After trapping, the particle can be released by simply reversing the sign of the applied voltage that causes electrophoretic forces on the particle in opposite direction.

Figure 2.3.3 shows voltage-dependence of ionic current distributions in the course of trapping/detrapping processes for the two particles. At every voltage condition, bimodal distributions were obtained, which indicates two dominant current state, I_{open} and I_{trap}, corresponding to the ionic current flowing through the open and clogged pore, respectively. The shape of the peak features are different because of the current decay after application of voltage of different polarity to switch from trapping to detrapping that causes current overshoot due to charging/discharging of the electrode double layer capacitance at the Ag/AgCl electrode-buffer interface. However, the difference of peak

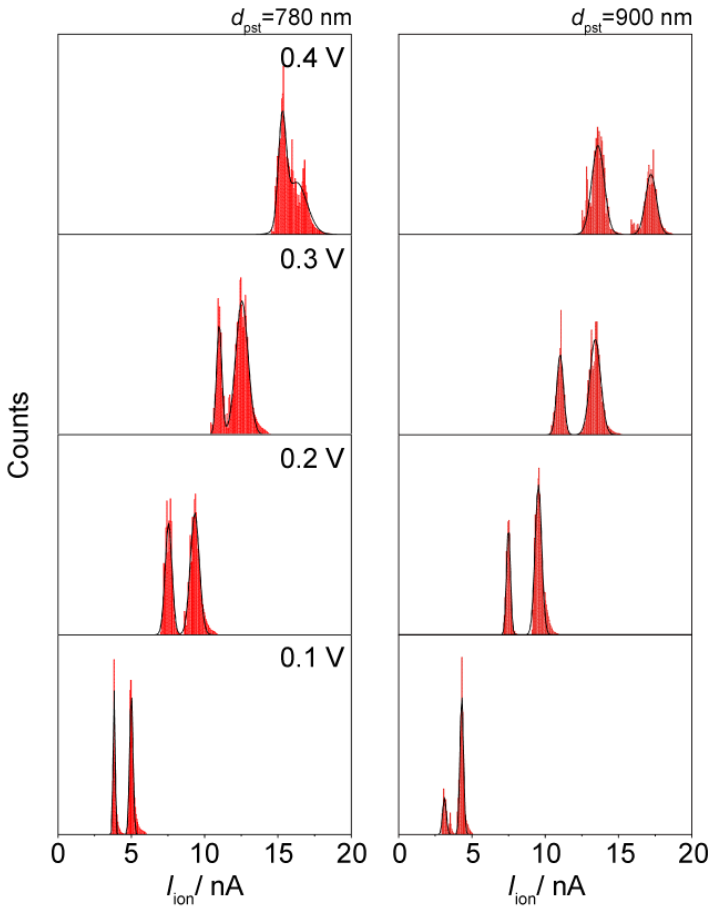

Figure 2.3.3. The histograms of ionic current in nanopore trapping method on the view of voltage and particle dependence.

values in each voltage for target particles indicated the possibility of discrimination between the particles by the difference of conductance under the effect of surface charge and the volume of analyte.

To evaluate the tendency between I_{open} and I_{trap}, the percentage of ionic current suppression was represented using the equation P_{trap}= 100(I_{open} - I_{trap})/ I_{open} for acquired peak values from the I_{ion} distributions (Figure 2.3.3). This result is shown in Figure 2.3.4. The linear shift was observed except for 900 nm microbead at V_b= 0.4 V. This tendency is useful for the interpretation of the particle in trapping. The complete sealing of a circular pore by a spherical particle leads to I_{trap} = 0. Therefore, there is a factor for the

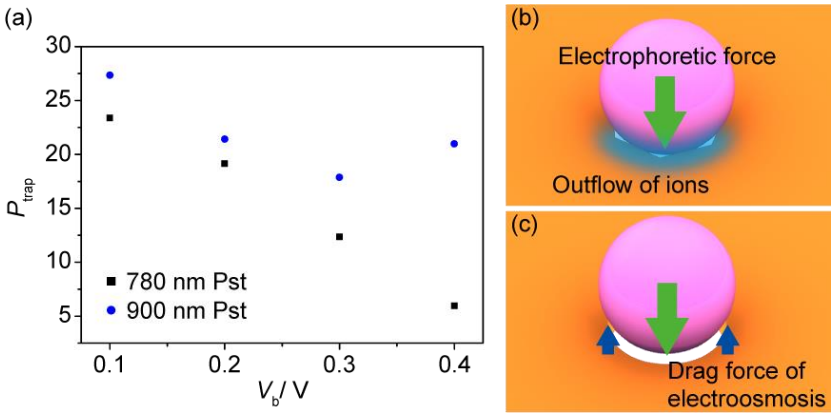

Figure 2.3.4. (a) The voltage dependence of P_{trap} about two diameter particles. (b), (c) Possible trapping which has some value of I_{trap}. The coherent trapping with outflow of ions due to irregular shape of a pore (b) and the particle floating attributed to the valance between electrophoretic force and drag force of electroosmosis (c).

value of I_{trap} such as the following: 1) the flow of ions after particle trapping due to the irregular shapes of a pore compared with an exact circle (Figure 2.3.4(b)) and 2) the particle floating at the vicinity of the pore because of the valance between electrophoretic force and drag force of electroosmosis (Figure 2.3.4(c)). In the complete blocking of the pore, P_{trap} would be zero. In addition, the case of Figure 2.3.4(b) would occur with vanishingly small compared with the electrophoretic flow. However, Figure 2.3.4(a) shows decreasing dependence of P_{trap} with voltage. It mean increasing of I_{trap}; moving away of the particle from the pore, therefore the particle under trapping are floating and receives stronger drag force of electroosmosis with voltage increasing. Considering this phenomenon from the view of analyte trapping, it reveals that the modulation of particle z-direct position by controlling bias voltage. However, the increasing of P_{trap} appears with 900 nm Pst at 0.4 V means the change of equilibrium of both force. Thus more investigations are needed for the accurate control of analyte position.

For the development of target discrimination, the nanopore trapping method is adopted to the mixture solution of two particles (Figure 2.3.2(b)). Trimodal histograms

were obtained. Each peak is ascribable to I_{open}, I_{trap} by the 780 nm-sized microbead (I_{trap1}), and I_{trap} by the 900 nm-sized microbead (I_{trap2}), respectively. For assignment, P_{trap} was derived from each value at V_b = 0.3 V. As a result, the two value; 11.2 and 21.7 were acquired as P_{trap1} and P_{trap2}, respectively. Compared with the individual measurement P_{trap} value in Figure 2.3.2(a), $P_{trap(700\ nm)}$ = 12.4 and $P_{trap(900\ nm)}$ = 17.9, the correspondence was observed. The difference of each P_{trap} values might be attributed to the employment of different devices.

In conclusion, in this section, voltage-specific discrimination via the difference of surface charge density using a nanopore trapping method was demonstrated. It was revealed that the particle flowing in trapping and this method could be useful to modulate z-direction position of analyte. Therefore this method are very suitable for the combination with other measurement system such as nanoelectrode.

Reference of this section

1. M. van der Hout, V. Krudde, X. J. A. Janssen, and N. H. Dekker, *Biophys. J.* **99**, 3840 (2010).

2. M. Tsutsui, Y. Maeda, Y. He, S. Hongo, S. Ryuzaki, S. Kawano, T. Kawai, and M. Taniguchi, *Appl. Phys. Lett.* **103**, 013108 (2013)

3. M. Belkin, S. -H. Chao, M. P. Jonsson, C. Dekker and A. Aksimentiev, *ACS Nano* **9**, 10598 (2015).

4. Y. He, M. Tsutsui, M. Taniguchi, and T. Kawai, *J. Mater. Chem.* **22**, 13423 (2012)

2.4. Nanopore trapping mechanism analysis via current measurement and fluorescent observation

In previous chapters, the different types of behavior in current drops were observed and utilized for acquiring targets' information. As just described, in almost nanopore experiment, occurrence of various events are interpreted via current shift only. However, there are many possible events, which can affect the pore conductance, e.g. translocation, fly-by event around the pore orifice, and trapping[1-3]. Therefore, the understanding about the relationship between occurring events and signals are one of the fundamental issue for realizing target analytes. Especially, it is of great importance to assure the presence of target at the pore at the moment of signal observation.

A usual method for the assurance of analyte existence around the pore is optical microscopic observation. One of the most attractive point of this approach is the visualization of dynamic motions of analytes around the pore. For instance, Mitsui and his colleagues[4] reported electrophoretic capture of single-molecule DNA into a nanopore by fluorescence observation alone. The motion of DNA was observed around the nanopore with the different gate voltages and presented the possibility for controlling the dynamics of analyte at the vicinity of a nanopore. Moreover, some groups have achieved analyte detection in translocation by simultaneous measurement via ionic current and fluorescence images[5-8].

In this section, to make sure the correspondence between the current signals and the actual events occurred, simultaneous measurements of fluorescence of dyed particles and the cross-pore ionic current is carried out. For this, a low aspect ratio solid-state nanopore was combined with a microfluidic channel for incorporating fluorescence microscopy.

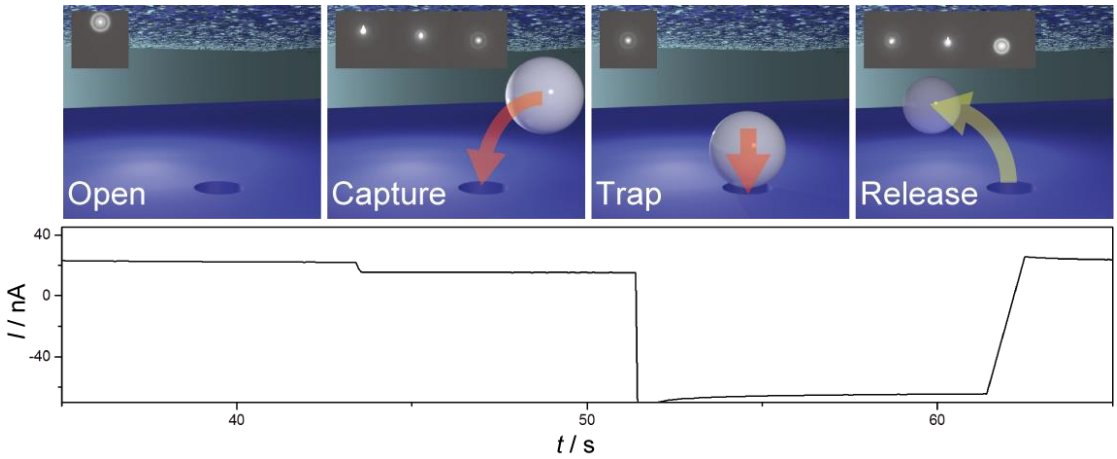

Figure. 2.4.1. The concept of electrical/optical measurement in nanopore trapping method.
The fluorescent image in trapping process and corresponding graphical image (up) and the current trace (bottom).

2.4.1. Fabrication of nanopore/microchannel devices for electrical/optical simultaneous measurements

Nanopore/microchannel devices for the electrical/optical measurements were fabricated through the following processes. A 4-inch silicon wafer constructed with three layers (SiN/Si/SiN = 50 nm/0.5 mm/50 nm) was utilized as a substrate. For electron-beam lithography, metallic markers (Ti/Au/Ti = 2 nm/30 nm/2 nm) were made on one side of the surface (front side) using photolithography and radio-frequency magnetron sputtering methods. After that, a small region of SiN of the other side (backside) was removed by another photolithography process and subsequent reactive ion etching using CF_4 as an etchant gas. This removed area, whereat Si layer was exposed, was contacted to an aqueous solution of KOH for anisotropic deep etching of the 0.5 mm thick Si to make 70 μm-square-sized 50-nm-thick SiN free-standing membrane. Then, the backside of the wafer except two circle regions was covered by a 50 nm-thick Cr by the sputtering. Furthermore, SU-8 was spin-coated on the front surface of the wafer to create micro-fluidic channels by a photolithography and this side also covered by a 50 nm-thick Cr by the sputtering. These Cr layer was used as etching mask to drill inlet and outlet holes for fluidic channel by deep Si etching using a Bosch process. After removing the Cr layers on the both sides by wet etching, the wafer was cut into small chips. Subsequently, another electron-beam drawing and reactive ion etching processes were used to make a 900 nm-sized pore in the SiN membrane. In measurements, the SU-8 channels were sealed with a coverslip using topcoat while polydimethylsiloxane (PDMS) block having a microchannel on one side was adhered on the other side of the nanopore chip. Finally, two Ag/AgCl electrodes were set in this block for adding electrophoretic voltage across the pore and measuring the cross-pore ionic current.

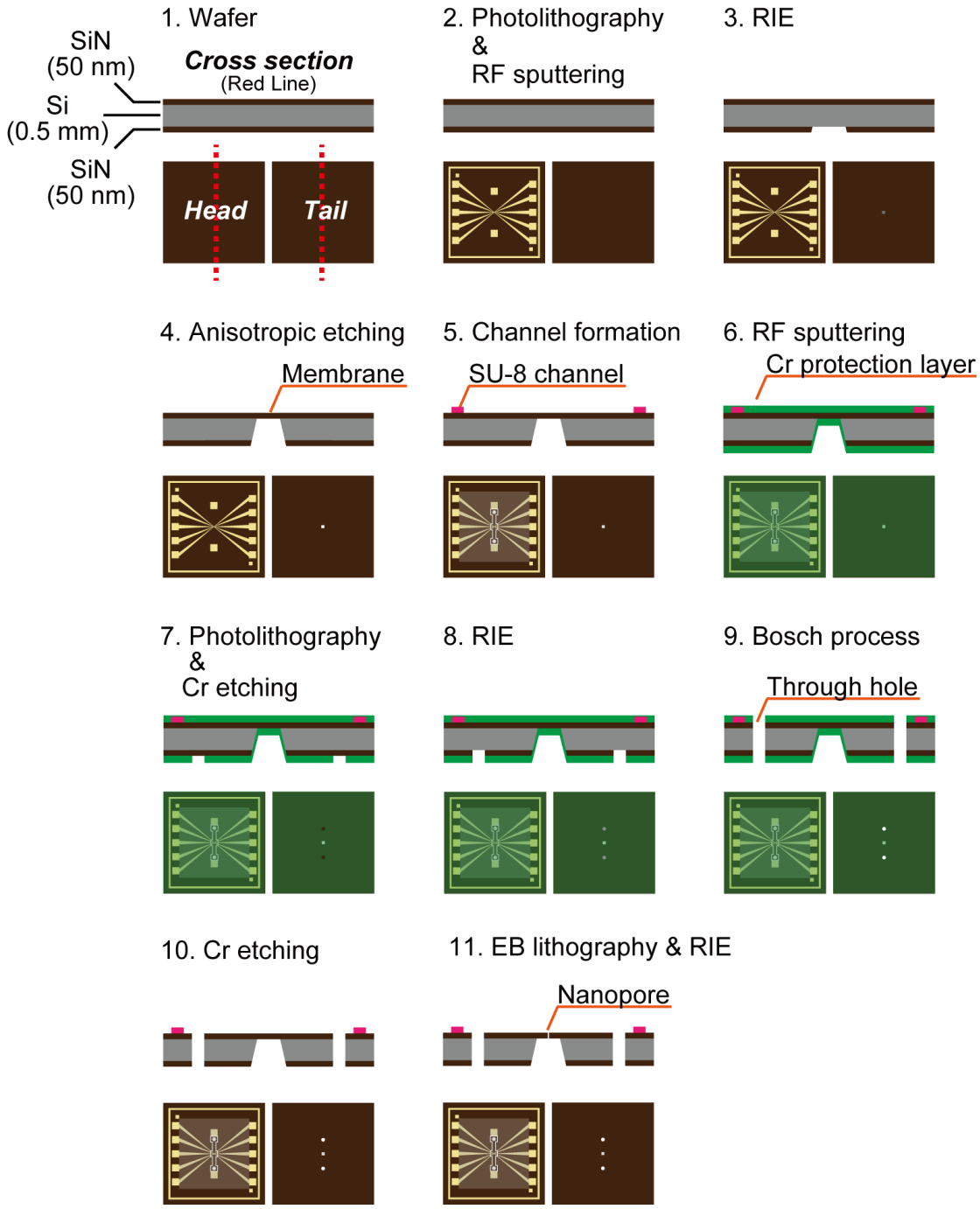

Figure. 2.4.2. Fabrication process of fluidic channel integrated nanopore device.

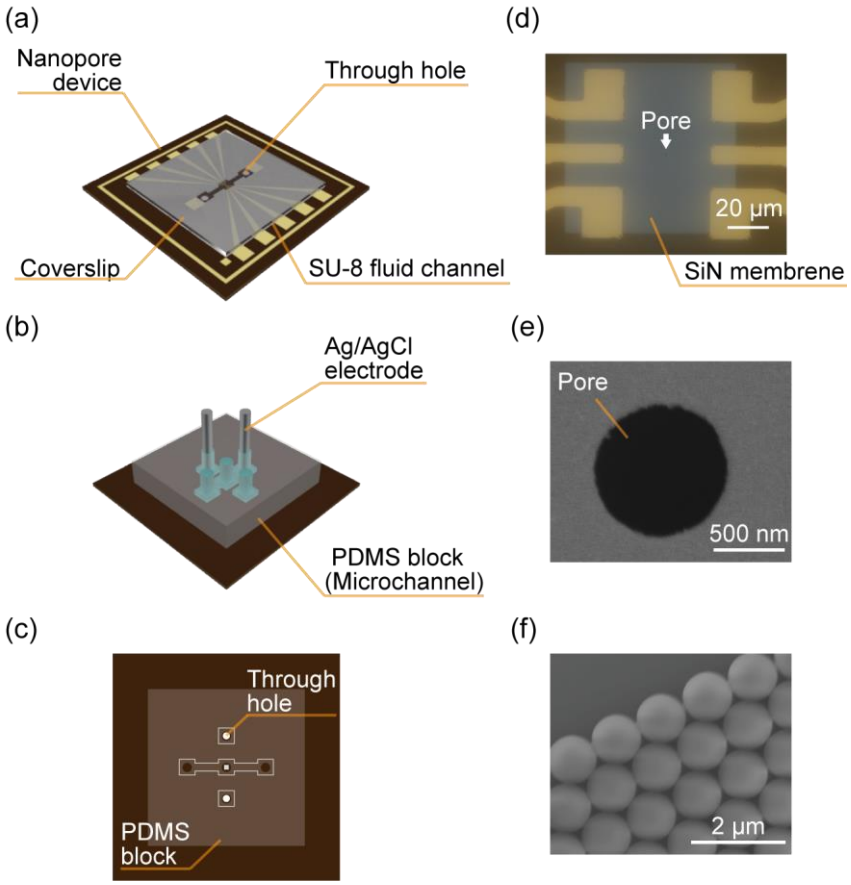

Figure. 2.4.3. Images of device and analyte. (a) Observation and (b), (c) measurement side of a simultaneous measurement device. The measurement side as seen from above. This device has (d) SiN membrane and (e) 0.9 μm-sized pore on the center. (f) Scanning electron microscopy (SEM) image of fluorescent particles served as analyte in this study.

2.4.2. Tracking particle trapping processes via electrical/optical measurements

Fluorescently-labeled polystyrene particles functionalized with COOH group purchased from Invitrogen (T8880) was used as analyte. This particles was dispersed into 1/100 diluted 10x PBS buffer (Wako Pure Chemical Industries, Ltd) at concentration of 0.4 ng/μL. The particle solution was introduced to the SU-8 channel via the backside PDMS microchannel and two through holes. Another microchannel formed on this block was filled with PBS buffer. These solution were contacted with the nanopore area. Therefore, analyte particles were present only at the observation side of the channel while the other side of the pore is filled only with buffer solution. The electrodes were connected to Keithley 6487 picoammeter/source for applying the electrophoretic voltage and recording the cross-pore ionic current. The trajectory of particles are tracked and recorded by using Olympus fluorescence microscope IX-73 equipped with an Andor ixon Ultra CCD camera with 0.033 s exposure time and 29.86 frames/s image capture rate.

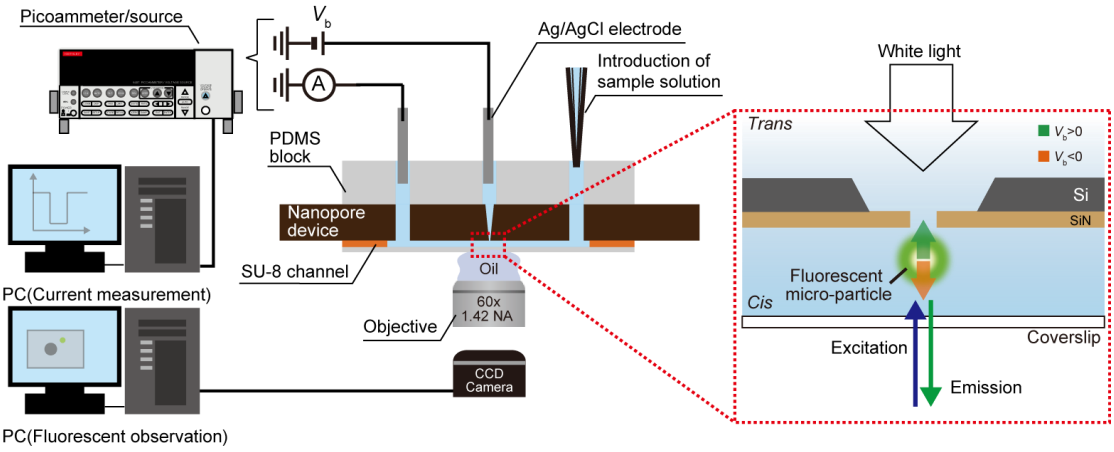

Figure. 2.4.4. Setup of simultaneous measurement.

2.4.3. The trajectory analysis in nanopore trapping method

Typical behavior of analyte in nanopore trapping method by the simultaneous measurement is shown in Figure. 2.4.5(a). In these traces, sudden drops of current to I_{trap} were observed. On the other hand, in the fluorescence observation, fluorescent particles, which has finite charges, under Brownian motion was observed. As described above, the thickness of SiN membrane (50 nm) is thin enough for light transmission and we can observe the micrometer region around the pore in optical images. The vertical focus was adjusted on the membrane, so there was a fringe at a free-moving particle. In particle tracing, same as electrical measurement, four types of events were observed; open pore, particle capture, and particle release by the change of the sign of applied voltage. This unambiguously ensures the presence of particles at the pore after I_{ion} drops to I_{trap}.

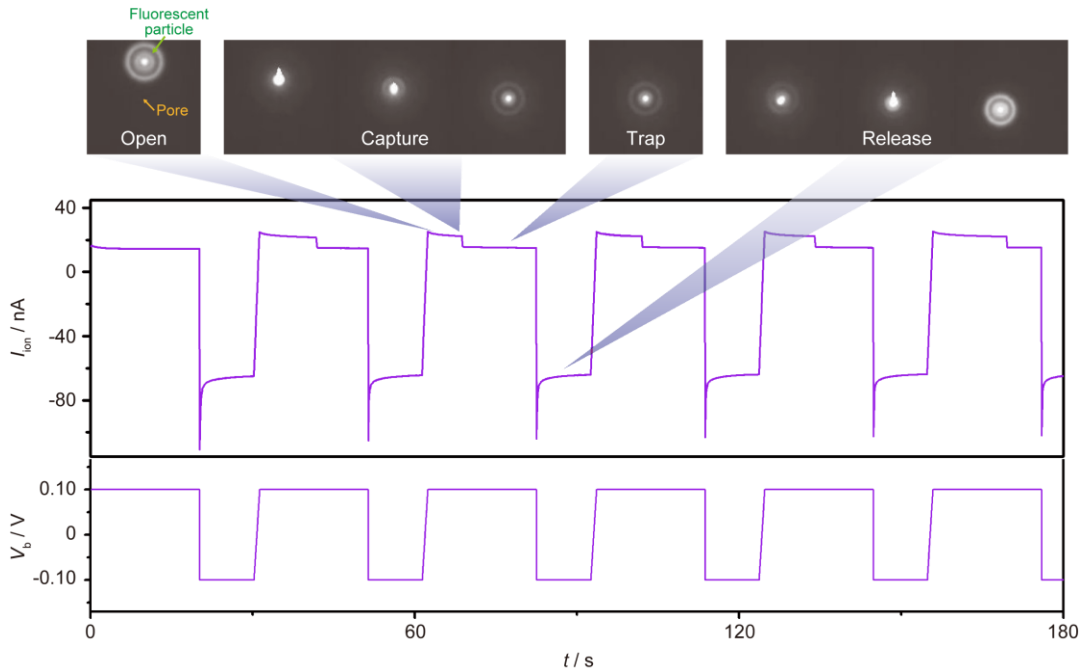

Figure. 2.4.5. Typical behavior of the particle and current curve correspond with voltage shift in the simultaneous measurement.

The further trapping mechanism was investigated in more detail by tracing several types of current shift. In the histogram constructed by the data from repetitive trapping/detrapping over 150 times showed bimodal distribution. It indicates various types of trapping events concerning particle positions. Assigning those distinct electrical signatures to the actual events is interesting (Fig. 2.4.6). In this optical/fluorescent measurement system, the scale of fluorescent image is derived from the comparison between these images and microscopic image of membrane. Figure 2.4.7(a) is the current trace from consecutive single particle trapping. In these 6th trial, only 5th sequence shows moderate decreasing in current compared with the other. On the other hand, in the

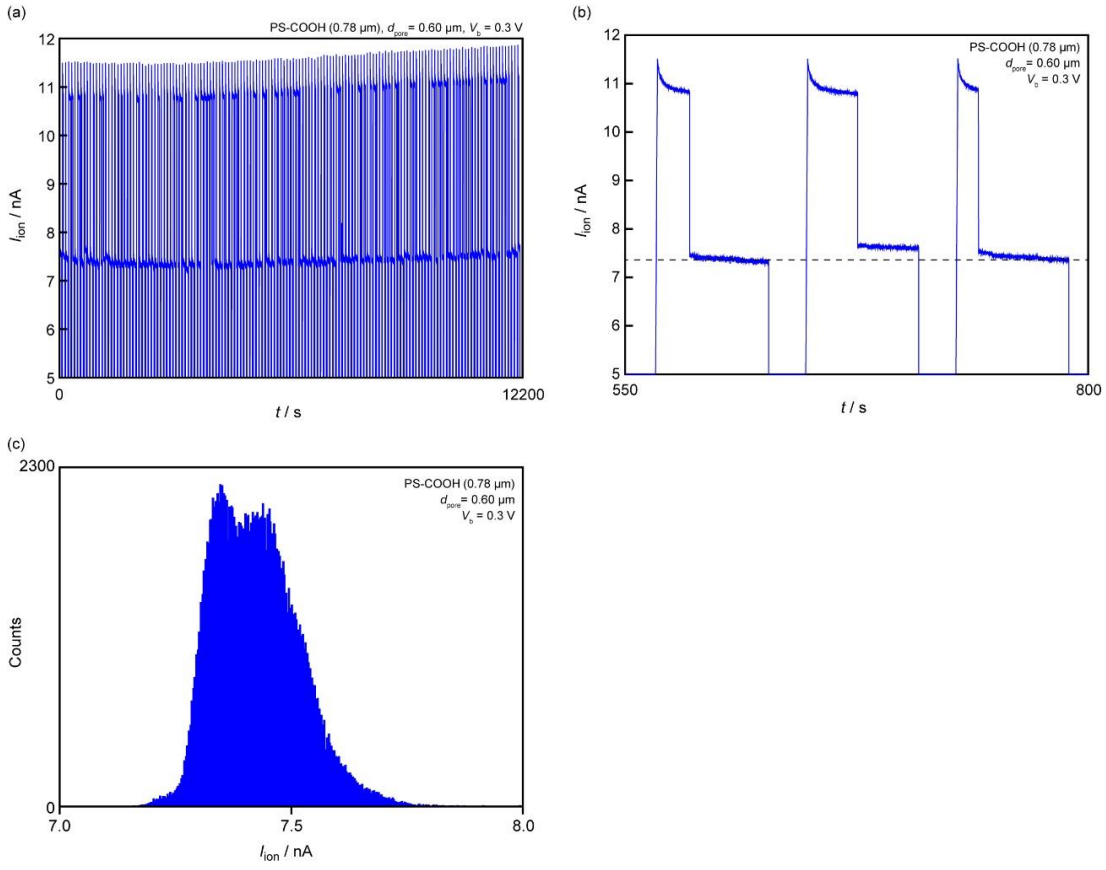

Figure. 2.4.6. The tendency of current trace over 150 in the nanopore trapping experiment using 600 nm-sized pore and 780 nm-sized COOH-modified particle (PS-COOH). (a) The whole current trace. (b) The difference of decreasing current amplitude by the trap. (c) The histogram constructed from the data of (a).

fluorescence image, each trapping position shows 590 nm-lateral difference only 5th one. This distance was derived from comparison between the position difference for center of bright point using the software Image J (National Institute of Health, USA, http://rsbweb.nih.gov/ij/). It indicates partial blocking by a particle provide more space for ionic conduction.

For acquiring further quantitative information on this difference, a Multiphysics simulation using COMSOL software was conducted. The resistance of open pore system composed by the three register in series is established; the cis chamber, the pore and the trans chamber. The access resistance of both chamber are same and represent following equation,

$$R_{\mathrm{acc}} = \frac{1}{4r} \cdot \frac{1}{e \sum_{\mathrm{i}} \mu_{\mathrm{i}} n_{\mathrm{i}} |z_{\mathrm{i}}|} \qquad (1)$$

where r is radius of nanopore, μ_{i} is the electrophoretic mobility of the i^{th} type of ions, ni is the imposed concentration of that type and z_{i} is the valance. On the other hand, pore resistance is,

$$R_{\mathrm{pore}} = \frac{L}{\pi r^2} \cdot \frac{1}{e \sum_{\mathrm{i}} \mu_{\mathrm{i}} n_{\mathrm{i}} |z_{\mathrm{i}}|} \qquad (2)$$

where L is the thickness of nanopore. For low aspect ratio nanopore such as one used in this dissertation, the access resistance become much larger than the pore resistance. Therefore in this numerical situation, the access resistance is considered in a careful way. However, in the approach using 3-dimensional finite-element simulation, the huge space of chamber become restriction of computing capacity. Therefore, the system modeled for this simulation is shown in Figure 2.4.7 and the resistance of shadowed area should be

$$R_{\mathrm{model}} = \left[\left(\frac{1}{4r} - \frac{1}{2\pi r_{\mathrm{up}}}\right) + \frac{L}{\pi r^2} + \left(\frac{1}{4r} - \frac{1}{2\pi r_{\mathrm{dn}}}\right)\right] \cdot \frac{1}{e \sum_{\mathrm{i}} \mu_{\mathrm{i}} n_{\mathrm{i}} |z_{\mathrm{i}}|} \qquad (3)$$

where r_{up} and r_{dn} are the radii of the up and down chambers, respectively. While resistance

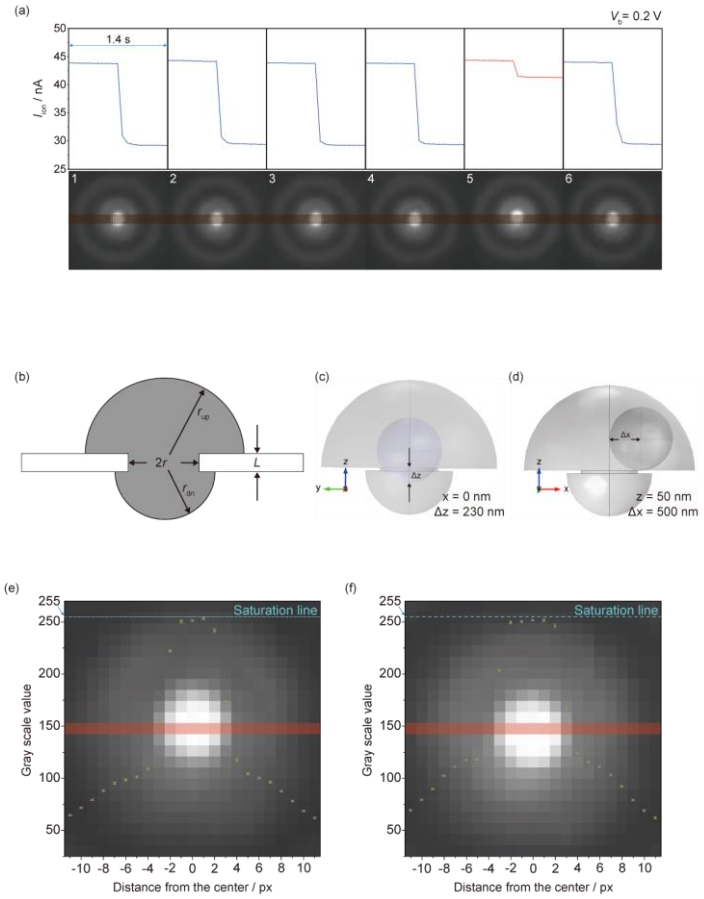

Figure. 2.4.7. (a) The trap positions and ionic current changes in consecutive trapping. The 5 th trapping showed different position in the fluorescent image with a small current drop. The brown band in fluorescent microscopic images is on the bright points for ease of viewing the particle position. (b) The model used for COMSOL simulation. (c), (d) The multiphysics calculation images for the particle trapped at the orifice of the pore and the different position from a center axis of the pore. (e) The magnified views and line profiles (green point) in 12 seconds about gray scale value of the fluorescent image for 4 th (I_{ion} dropped by more than 10 nA) and (f) 5 th (I_{ion} dropped by only several nA) events corresponding to the models of (c) and (d), respectively. The horizontal axis indicates the pixel distance from center of a particle and the red band in images is the focused area.

of the space outside of shadowed area should be

$$R_{\text{outer}} = \left[\frac{1}{2\pi r_{\text{up}}} + \frac{1}{2\pi r_{\text{dn}}}\right] \cdot \frac{1}{e\sum_{\text{i}} \mu_{\text{i}} n_{\text{i}} |z_{\text{i}}|} \qquad (4)$$

In this numerical simulation, only shadowed area was considered and put voltage difference ΔV on the two arc ends of the hemispheres:

$$\Delta V = V_{\mathrm{b}} \cdot \frac{R_{\mathrm{model}}}{R_{\mathrm{outer}}+R_{\mathrm{model}}} \quad (5)$$

Then, the ionic current was numerically calculated through this system. By tuning the quantities of r_{up} and r_{dn}, numerical value of the current which matches with the analytic one were finally obtained:

$$I = \frac{V_{\mathrm{b}}}{2R_{\mathrm{acc}}+R_{\mathrm{pore}}} \quad (6)$$

In this way, a finite-sized system which approximates the ideal system with infinite large chambers is established. In this calculation, applied voltage, diameter and thickness of a pore are adopted V_{b}= 0.2 V, d_{pore}= 900 nm and L = 50 nm, respectively. In addition, main solute concentration of buffer as NaCl = 13.70 mM was utilized. In the setting r_{up} = 3r and r_{dn}=1.5r, the results match. When a particle exist in the system, the voltage falling in the above space as seen in Eq. 5 is assumed firstly the electrical current I_0 was numerically calculated. Since in the above process, the resistance of the simulated area is approximated by the open pore situation shown in Eq.3, while the actual resistance should be

$$R_{\mathrm{block}} = \frac{\Delta V}{I_0} \quad (7)$$

Therefore, the voltage drop in this simulated region should be re-evaluated as:

$$\Delta V_{\mathrm{block}} = V_{\mathrm{b}} \cdot \frac{R_{\mathrm{block}}}{R_{\mathrm{outer}}+R_{\mathrm{block}}} \quad (8)$$

Then the ionic current is re-calculated using the above renewed voltage values. By using this approach, the current blockage by a particle positioned at the pore orifice was estimated. As a result, when particle blocks the pore at the center with distance between the pore orifice and the particle edge Δz is about 230 nm, the current blockade ΔI is about 15 nA (Figure 2.4.7(c)). On the other hand, when the particle position derives from the center of the pore Δx by = 500 nm, ΔI was as small as 3 nA (Figure 2.4.7(d)). These result

are in good agreement with the experimental ones. These results indicate that floating of the particle above the pore due to the interplay of two opponent forces, electrophoretic force and electroosmosis drag force. Considering that any behavior of Brownian motion is not observed in current traces (as increase in the noise level) after trapping, it is envisaged that the motion of the particles are restricted strictly and virtually frozen under the equilibrium Δx and Δz via strong force. The amplitude of Brownian motion of this particle without condition electrophoresis could be calculated using Einstein-Stokes equation $D = k_B T/3\pi\eta d$ where D, k_B, T, η, and d are diffusion coefficient, Boltzmann constant, temperature, viscosity of solution and particle diameter, respectively. In this measurement, under the assumption of two-dimensional diffusion, the movement of particle by Brownian motion in 1 second are calculated as about 4 micrometer. Therefore nanopore trapping method is very useful for capturing of target. In addition, the possibility of modulation of target z-direction position are shown in section 2.3. Thus combination of these factors are might be excellent technique for controlling dynamics of analyte.

Under the simulation result of the floating particle in trapping, it is interesting to characterize the amplitude of fluctuation in a positon about frozen particle on the pore. Here, the line profile along the trapped nanoparticle are tracked for fluorescence images (Figs 2.4.7(e)-(f)). In these profiles, the three-dimensional fluctuations of the particles are represented as the variation of the amplitude of image contrast from 0 to 255. Comparing two results about two cases which showed I_{ion} drop with more than 10 nA and several nA (Fig. 2.4.7(a)), corresponding to a particle trapped at the center and that with nanoscopic distance from the center, respectively. The slight deviation found in the one images showed more out-of-focus indicates its higher position from the pore in agreement with the simulation. Besides, the fluctuations of the particles are within the negligible small

range of the spatial resolution of the microscopic observation system.

Conceivable factors, which may contribute to the different particle positions observed in the Fig. 2.4.7(a), are the hydrodynamic flow and the pore wall-particle interactions. The latter is attributed to van der Waals interaction between the pore wall and the particle. However, this is unlikely as such adhesive force are usually strong enough to make an eternal bind the particle on surface in contrast to the fluorescent observation where trapped particle can be released easily via the change of voltage sign. Rather, it is more likely to that electroosmosis plays an important role; occurs opposite direction flow to the electrophoresis and therefore acts to repel the particle from the pore[10-11]. Considering that electroosmotic flow could occur significantly only in the nanometer vicinity of the pore wall, in general, little or strong drag force of this flow was applied to a microbead when it approaches straight or at angle to the pore, respectively. Thus, it is speculated that the small current blockade is due to a particle came from a side to the pore wherein it experienced strong hydrodynamic forces and be inhibited from being captured in the center.

In addition to the trapping concerning single-particle, the trap of double particles captured together was observed. In the current trace shown in Figure 2.4.8, two-staged current drop can be seen and denoted as trap A and trap B. At the same time, in the fluorescence observation, consecutive trapping of two particles were observed (A in Fig. 2.4.8(a) and (b)). The capture of second particle means that electric field outside the clogged pore, therefore corroborating the incomplete blockade by the particle most likely floating the pore by the electroosmotic flow. Furthermore, the amplitude of the current shift was quite small for the second trap compared with the first one. This also suggests that the first particle occupied large area of pore orifice so that subsequent trapping could

not block the ionic flow further. This simultaneous measurement reveals that the origin of multiple-stage current drop is not due to the sudden shift of particle position occurred by a single particle but multiple ones.

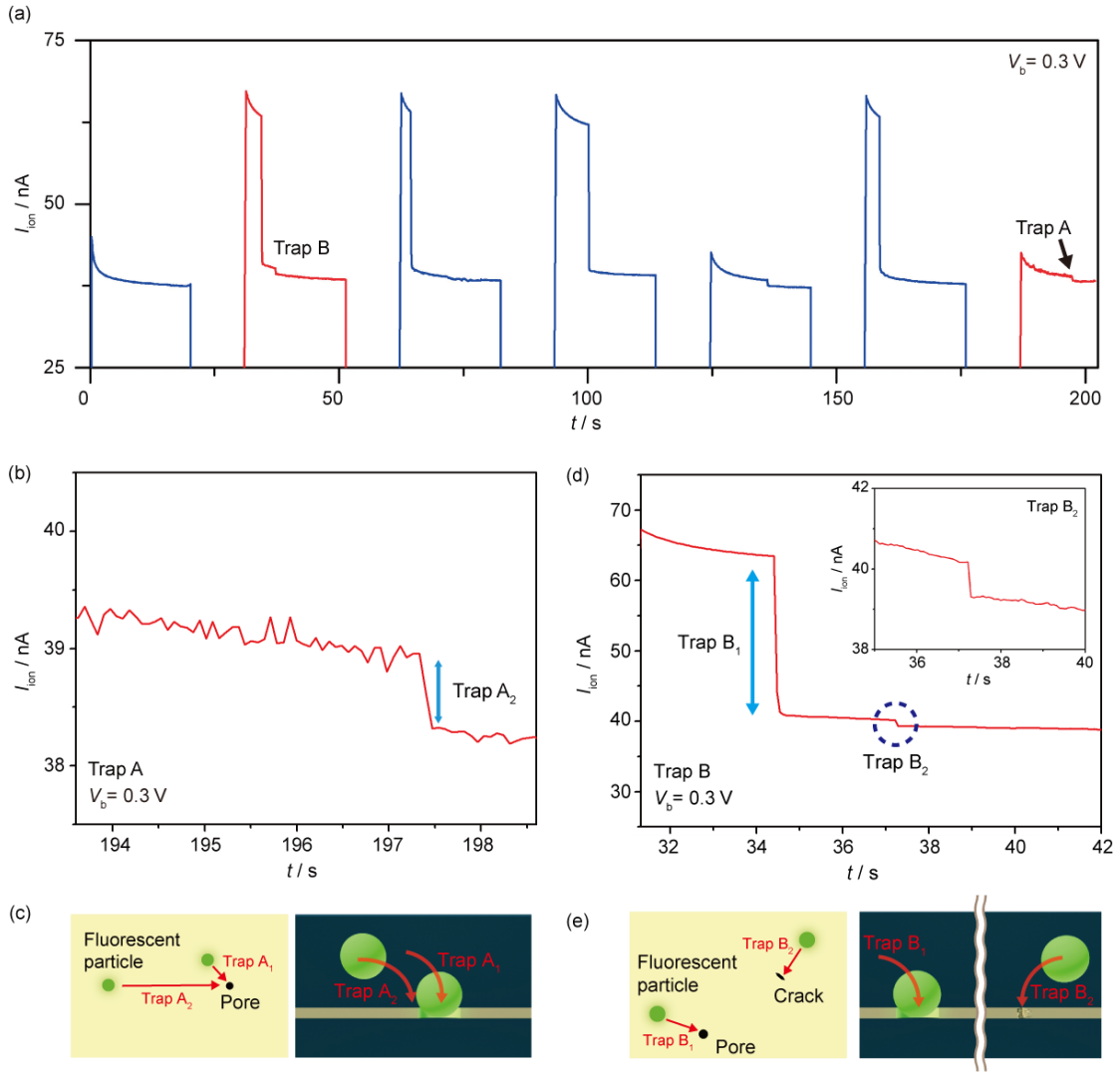

Figure. 2.4.8. (a) Ionic current trace showing multi-particle trapping events. (b) Magnified view of Trap A in (a). Only trapping of the second particle (Trap A_2) is detected. (c) Schematic model about Trap A. (d) Current decrease during Trap B in (a). Large (Trap B_1) and small (Trap B_2; the inset of this graph) drops were observed, which were attributed to (e) trapping into the original pore and the nano-crack, respectively.

Finally, an interesting feature was found; the trapping in the place other than the pore. At the same time, the I_{ion} trace showed that a small shift upon the peculiar trapping (Fig. 2.4.8(d)). This unexpected trapping therefore indicates that occurrence of a nanopore unintentionally generated in a membrane. Yanagi[12] and his colleagues reported that dielectric breakdown in the SiN membrane via voltage pulsing induces creation of nanopores. Since the membrane would be under an electrical stress in a similar way by the repeated voltage change for trapping/detrapping process, it is probable that a nanoscale crack was formed during the measurements. It is also possible that the irrelevant pore was generated in the fabrication processes. For certain, fluorescent images revealed that the particle trapped in the nano-crack showed higher trapping position compared with designed pore and it implies weaker electrophoretic force to drawn the particle (Figs. 2.4.9(a) and (b)). In conventional nanopore measurement, the weak electrical signals was interpreted as the double trap described above or a fly-by process around pore orifice. In sharp contrast, this electrical/optical measurements revealed that

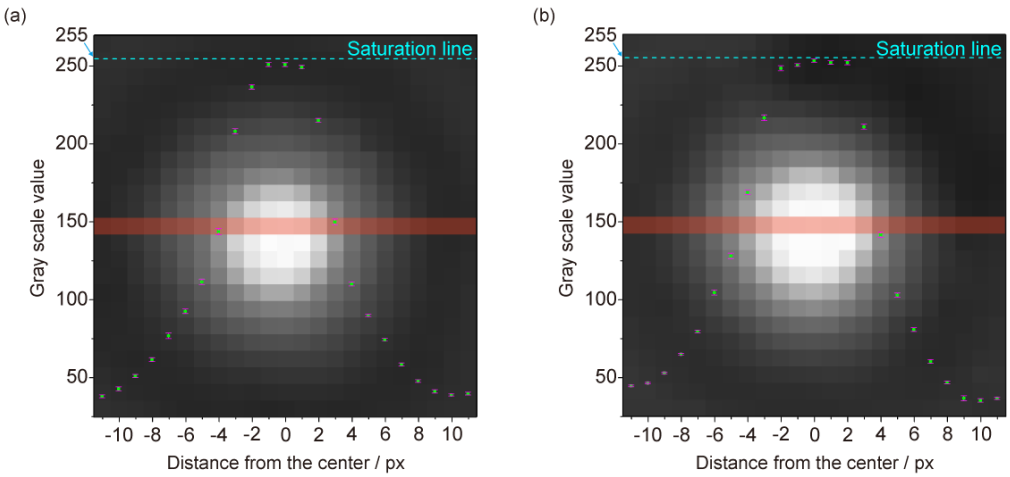

Figure. 2.4.9. The magnified views and line profiles (green point) for gray scale value in 12 seconds about Trap B_1 (a) and Trap B_2 (b). The horizontal axis is the pixel distance from center of a particle and the red band in images is the focused area.

I_{ion} steps would also be attributed to a particle capture at defective sites in the membrane.

In this section, as conclusion, simultaneous measurement of fluorescence and ionic current using a novel device configuration of microchannel and nanopore was demonstrated. It was found that this method is useful for studying unknown features in the ionic current curves by evaluating the detail mechanism in nanopore trapping as well as discovering unexpected capture events and its correspondence to the behavior of current shift. The combination of single particle dynamics and ionic current signals would be useful for exploring new sensing methods using nanopores and nanoelectrodes.

Reference of this section

1. A. Carlsen, O. Zahid, J. Ruzicka, E. Taylor and A. Hall, *ACS Nano* **8**, 4754 (2014).
2. A. Arima, M. Tsutsui and M. Taniguchi, *Appl. Phys. Lett.* **104**, 163112 (2014)
3. S. W. Kowalczyk and C. Dekker, *Nano Lett.* **12**, 4159 (2012)
4. G. Ando, C. Hyun, J. Li and T. Mitsui, *ACS Nano* **6**, 10090 (2012)
5. V. V. Thacker, S. Ghosal, S. Hernández-Ainsa, N. A. W. Bell and U. F. Keyser., *Appl. Phys. Lett.* **101**, 223704 (2012)
6. V. Kurz, E.M. Nelson, J. Shim and G. Timp, *ACS Nano* **7**, 4057 (2013)
7. N. Yukimoto, M. Tsutsui, Y. He, H. Shintaku and S. Tanaka, *Sci. Rep.* **3**, 1855(2013)
8. A. Ivankin, R. Y. Henley, J. Larkin, S. Carson, M. L. Toscano and M. Wanunu, *ACS Nano* **8**, 10774 (2014)
9. R. Marchand, F. Carcenac, L. Malaquin, E. Trévisiol, C. Vieu and C. Thibault, C. *Microelectron. Eng.* **144**, 57 (2015)
10. Bacri, L.; Oukhaled, A. G.; Schiedt, B.; Patriarche, G.; Bourhis, E.; Gierak, J.; Pelta, J.; Auvray, L. *J. Phys. Chem. B* **115**, 2890 (2011)
11. van Dorp, S.; Keyser, U. F.; Dekker, N. H.; Dekker, C.; Lemay, S. G. *Nat. Phys.* **5**, 347 (2009)
12. Yanagi, I.; Akahori, R.; Hatano, T.; Takeda, K. *Sci. Rep.* **4**, 5000 (2014)

Chapter 3 Nanogap electrode system for single-biomolecular analysis

Introduction

In the previous chapter, nanopore analysis via ionic current measurement was conducted. In these measurement, the behavior of ions under the effect of field and analyte appears as the shift of current. We acquire the information concerning analytes, such as the size and the surface charge density, from the current change directly. In this approach, the extended-nanospace inside a nanopore served as virtual electrodes to identify an analyte residing inside the pore.

On the other hand, an alternative way is to attach two pieces of electrodes directly to biomolecules and measure the current flowing through them. The recent progress of nanotechnology has enabled to make such ideal situation a reality in laboratory.[1] One of the promising tool useful for this purpose is a mechanical break junction method.[2,3] In this method, a metal wire is stretched mechanically and broken to create two electrodes with close separation. The gap distance between the electrodes is further adjusted by a mechanical control to fit the size of a target molecule of interest. In the measurement, a pair of electrodes are formed by this procedure and the tunneling current flowing through the electrodes is measured in a liquid containing the molecules. Then, when a molecule is trapped between the electrodes, one can obtain the single-molecule conductance, from which various electrical properties intrinsic to those molecules can be estimated such as the highest occupied molecular orbital (HOMO) and the lowest unoccupied molecular orbital (LUMO) levels.[4] As any molecules have distinct electronic structure unique to them, the tunneling current measurements allow single-biomolecule discriminations.[5-7]

To date, such measurements are conducted by many research institutes and companies that aim to develop next-generation DNA sequencer.[8-10] This method are based on the difference of the single-molecule conductance among the four nucleotides. As no labelling of molecules is necessary in this electrical approach, the method is considered as one of the promising single-molecule techniques for fast and low-cost genome sequencing. Recent experiments have extended the measurements to sequencing of peptides opening a venue for the applications in proteomics.[11]

In this chapter, a nanogap electrode system is developed for electrical detections of single-proteins via two-probe current measurements. Here, a special care is taken to cover the electrodes with insulating layer for minimizing ionic current that often cause a large noise whereby degrading signal-to-noise ratio for single-molecule identification. For this, a SiO_2-covered free-standing Au nanowire is fabricated on a polyimide layer coated phosphor bronze substrate. By breaking the SiO_2/Au wire through mechanical deflection of the metal beam, a pair of Au electrodes with close separation is formed whose entire surface except the fresh fracture surface is fully-protected by the SiO_2 layer. The insulator-protected nanogap electrodes are used for measuring current through single-proteins in buffer at room temperature for verifying the feasibility to discriminate proteins by the molecular structure.

Besides, using this insulator-protected electrodes, the discrimination of proteins was implemented in liquid conditions. In this research, the feature of structure and electric transfer of proteins were focused. This approach can in principle provide novel information of proteins under in vivo environment.

Reference of introduction

1. H. Song, M. A. Reed, T. Lee, *Adv. Mater.* **23**, 1583 (2011)
2. M. Taniguchi, M. Tsutsui, K. Yokota, and T. Kawai, *Nanotechnology* **20**, 434008 (2009)
3. M. Tsutsui, K. Matsubara, T. Ohshiro, M. Furuhashi, M. Taniguchi, and T. Kawai, *J. Am. Chem. Soc.* **133**, 9124 (2011)
4. L. A. Bumm, J. J. Arnold, M. T. Cygan, T. D. Dunbar, T. P. Burgin, L. Jones II, D. L. Allara, J. M. Tour, and P. S. Weiss, *Science* **271**, 1705 (1996)
5. L. Venkataraman, J. E. Klare, C. Nuckolls, M. S. Hybertsen, M. L. Steigerwald, *Nature* **442**, 904 (2006)
6. X. Xiao, B Xu, N. J. Tao, *J. Am. Chem. Soc.* **126**, 5370 (2004)
7. J. He, F. Chen, J. Li, O. F. Sankey, Y. Terazono, C. Herrero, D. Gust, T. A. Moore, A. L. Moore, and S. Lindsay, *J. Am. Chem. Soc.* **127**, 1384 (2005)
8. M. Tsutsui, M. Taniguchi, K. Yokota, and T. Kawai, *Nat. Nanotechnol*. **5**, 286 (2010)
9. S. Huang, J. He, S. Chang, P. Zhang, F. Liang, S. Li, M. Tuchband, A. Fuhrmann, R. Ros, and S. Lindsay, *Nat. Nanotechnol.* **5**, 868 (2010)
10. M. Krems, M. Zwolak, Y. V. Pershin, and M. Di Ventra, *Biophys. J.* **97**, 1190 (2009)
11. T. Ohshiro, Ma. Tsutsui, K. Yokota, M. Furuhashi, M. Taniguchi and T. Kawai, *Nat. Nanotechnol.* **9** 835 (2014)

3.1. Nanogap electrode measurement

In addition to a molecular-sized electrode gap, an extreme stability of experimental set up to hold the extended-nanospace between electrodes for prolong time is required for single-molecule electrical measurements as even an Angstrom change in the inter-electrode distance would result in an order of magnitude change in the current due to its exponential dependence on the tunneling distance. Break junction methods are power tools widely utilized for this purpose.[1-6] Among the various versions of the techniques developed so far, STM-break junctions[1,2], electromigration break junctions, [3,4] and mechanically-controllable break junctions[5-6] are proven to be reliable in studying single-molecule electron transport. These three methods have their own merits and demerits. STM-break junctions utilize a STM probe tip and a metal substrate. This method provides an easy way of repeating junction breaking and formation through mechanical motion control of the probe. However, the mechanical stability of the system is often problematic as thermal drift would cause inadvertent change in the electrode gap size during the measurement.

On the other hand, electromigration break junction method can be used to form an electrode nanogap with excellent stability. In this method, a thin metal wire is lithographed on a substrate and voltage is applied to induce electromigration at the narrowest constriction that eventually lead to electrical breakdown. By finely controlling the voltage stress during the electrical breaking processes, one can form a pair of nanoelectrodes with sub-nanometer separation. Although this breaking procedure can create a robust nanogap electrode structure, one needs to compromise the gap size controllability as the electrode position cannot be altered after the wire rupture unless any

other treatment such as electroplating is performed.

Whereas the two methods can be viewed as extreme cases, MCBJ technique possesses characteristics suitable and useful for single-molecule conductance measurements.[7] By using a free-standing metal nanowire fabricated on a flexible substrate, one can form a pair of electrodes by breaking the wire through the bending control. The advantage of this mechanical junction method is that the ratio between the displacements of the electrode position and the amount of substrate deflection r can be made lower than 10^{-3} by the experimental set up configurations. Specifically, r is described as $r = 6ut/L^2$, where u, t, and L are the free-standing length of the junction, the thickness of the substrate, and the distance between the counter supports, respectively. As noted in the equation, nano-fabricating the junction structure to obtain smaller u provides lower r and hence better controllability of the inter-electrode gap distance through the substrate bending. Another strong point is that influence of the external vibration on the electrode stability is also damped by r. Overall, MCBJ method enables an easy way of forming electrode gaps mechanically tailored to fit the size of the test molecules of interest with excellent stability to hold the atomic-scale distance for enough long time even at room temperature in liquid.

The excellent properties of MCBJs have been in fact exploited in measuring single-molecule conductance for attaining better understanding of electron transport in metal-molecule-metal systems to realize single-molecule building blocks for future nanoelectronics. Recent experiments have proven that the method is also useful in identifying biomolecules such as DNA, RNA in liquid.[8-9] In these works, it was demonstrated that the single-biomolecules can be detected and discriminated by probing the tunneling current flowing through the molecules. Nevertheless, it was also observed

that the signal-to-noise ratio cannot be made high as the electrical noise in a liquid is relatively large compared to the picoampere tunneling current flowing through the molecules. Thus, in the present study, a SiO_2-coated MCBJ is fabricated for creating insulator-protected electrodes for the single-biomolecule detections in a liquid. Here, the insulator layer is intended to be used for suppressing ionic current to lowering noise level.

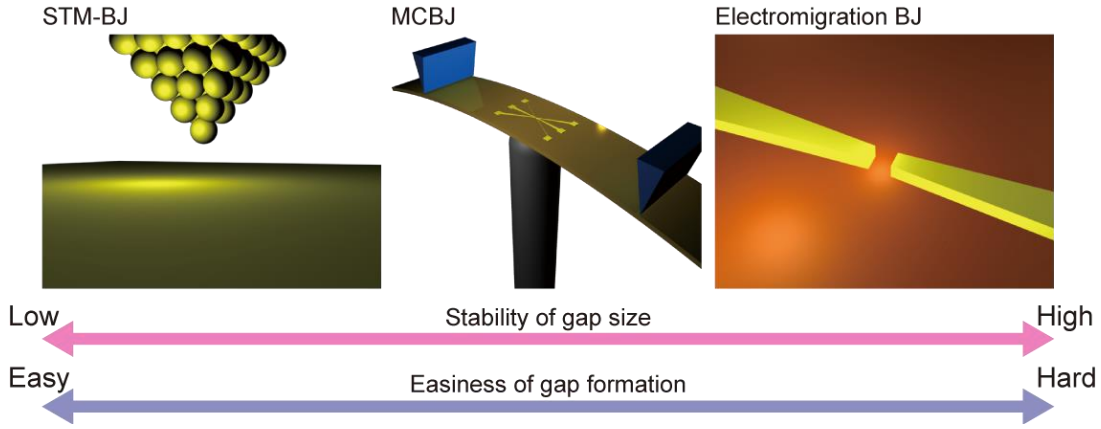

Figure 3.1.1. The comparison of nanogap-fabrication methods.

Reference of this section

1. N. J. Tao, *Nat. Nanotechnol.* **1**, 173 (2006).
2. M. Kiguchi, T. Ohto, S. Fujii, K. Sugiyasu, S. Nakajima, M. Takeuchi, and H. Nakamura, *J. Am. Chem. Soc.* **136**, 7327 (2014)
3. M. L. Trouwborst, S. J. van der Molen, and B. J. van Wees, *J. Appl. Phys.* **99**, 114316 (2006)
4. D. R. Strachan, D. E. Johnston, B. S. Guiton, S. S. Datta, P. K. Davies, D. A. Bonnell, and A. T. C. Johnson, *Phys. Rev. Lett.* **100**, 056805 (2008)
5. S. Huang, J. He, S. Chang, P. Zhang, F. Liang, S. Li, M. Tuchband, A. Fuhrmann, R. Ros, and S. Lindsay, *Nat. Nanotechnol.* **5**, 868 (2010)

6. M. Tsutsui, K. Matsubara, T. Ohshiro, M. Furuhashi, M. Taniguchi, and T.Kawai, *J. Am. Chem. Soc.* **133**, 9124 (2011)
7. N. Agraït, A. L. Yeyati, and J. M. van Ruitenbeek, *Phys. Rep.* **377**, 81 (2003).
8. M. Tsutsui, M. Taniguchi, K. Yokota, and T. Kawai, *Nat. Nanotechnol*. **5**, 286 (2010).
9. T. Ohshiro, Ma. Tsutsui, K. Yokota, M. Furuhashi, M. Taniguchi and T. Kawai, *Nat. Nanotechnol.* **9**, 835 (2014)

3.2. Investigation of insulator-sandwiched nanogap electrodes

In the past decades, electron transport through single-molecules has been widely studied with intent to develop molecular building blocks for future nanoelectronics.[1-5] The electrical properties of metal-molecule-metal junctions can be researched by using a break junction technique; in this method, a pair of electrodes with a nanometer gap for a single-molecule conductance measurement was created by mechanical breaking of a contact formed between two metals.[1-6] In particular, the device consists of a pair of free-standing nanoelectrodes for sensing current, and their relative position can be adjusted to fit the size of target analyte. Since these electrode are bare and not covered with any insulating materials, however, large background ionic current is detected in single-biomolecule detection because of the millimeter-scale surface area touching with electrolyte solution.[7,8] While this background current could be subtracted for extracting tunneling current change associated with single-molecule transmitigation through an electrode gap,[7,8] the ionic transport should be suppressed to attemper electrical noise and simplify the interpretation of electrical signatures.[9]

In this section, therefore a novel junction configuration having the whole area of metal electrode is sandwiched by an electrically-insulating material is fabricated. We could form dielectric-protected Au electrodes with fresh clean nanometer-scale sensing area touching with electrolyte solution adequate for single-biomolecule measurements (Fig. 3.2.1.). This nanostructure cannot be fabricated by conventional nano-fabrication techniques alone such as electron-beam lithography since it needs atomic-scale spatial resolution to achieve insulating cover to whole electrode area except electrode nano-scale edges. Herein, we investigated the electrode gap size dependence of the tunneling

current decay in various environments by using insulator-protected MCBJ device to demonstrate their capability for making a well-defined electrode gap and detecting tunneling current through the nano-scale electrodes.

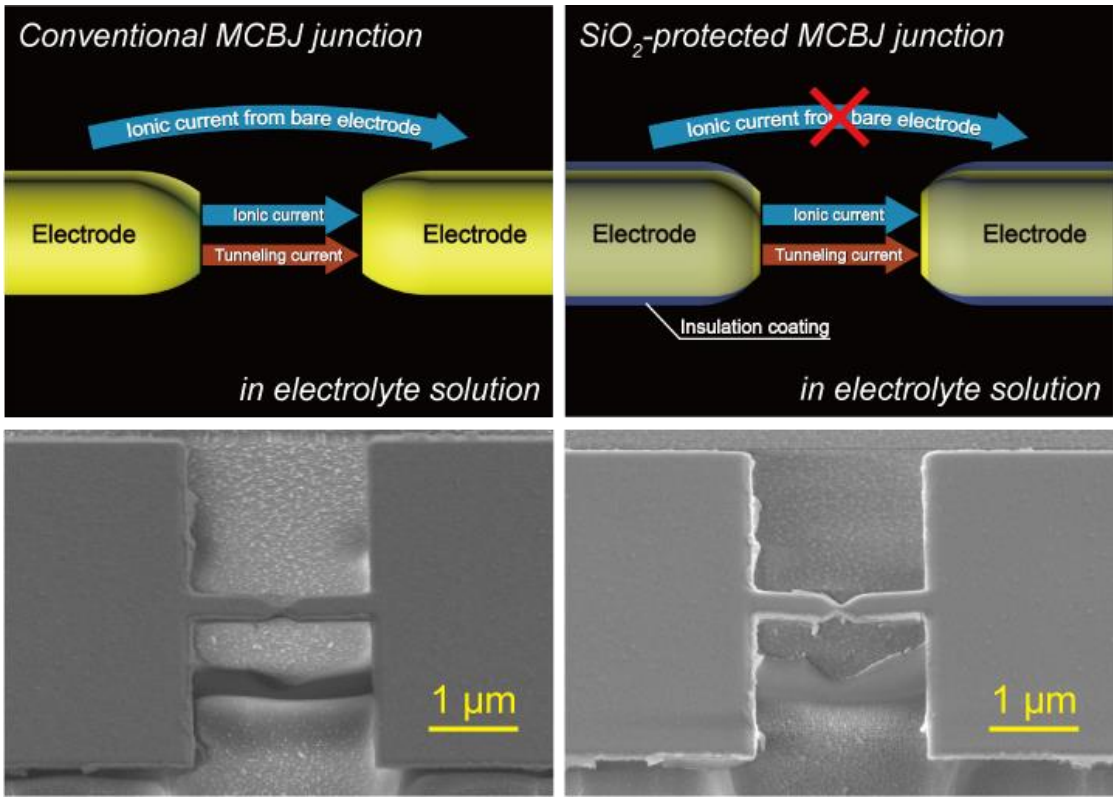

Figure 3.2.1. The conceptual and SEM images of conventional and SiO_2-protected MCBJ junctions.

Figures 3.2.1 to 3.2.3 are reproduced from *J. Appl. Phys.* 115, 114310 (2014) with the permission of AIP publishing

3.2.1. Fabrication of insulator-protected MCBJ devices

SiO_2-sandwiched free-standing Au junctions were fabricated through the processes described in the following. A mirror-polished phosphor bronze plate (8 mm×50 mm× 0.5 mm) was used as a substrate. Polyimide precursor was spin-coated and polymerized by several-step baking at up to 200 degrees Celsius. The first layer of SiO_2 (25 nm) was deposited by chemical vapor deposition (CVD) technique following the metallic marker construction by photolithography technique and RF magnetron sputtering. Then, an electron-beam lithography technique and RF magnetron sputtering were used to make an Au nanoelectrode. After that, RIE was used for making free-standing junction configurations following CVD to cover whole area by second SiO_2 layer except wiring points. The wires were connected to the junction using silver-based conductive paste CN-3160L (KAKEN TECH CO., LTD.) and epoxy encapsulant STYCAST 2850FT-J (Henkel AG & Co. KGaA).

The sensing area of this device appears by breaking the SiO_2-protected metal junction by to the MCBJ technique, which creates clean fracture surface for tunneling current measurements. Meanwhile, the SiO_2 layer largely suppress ionic current during the measurements.

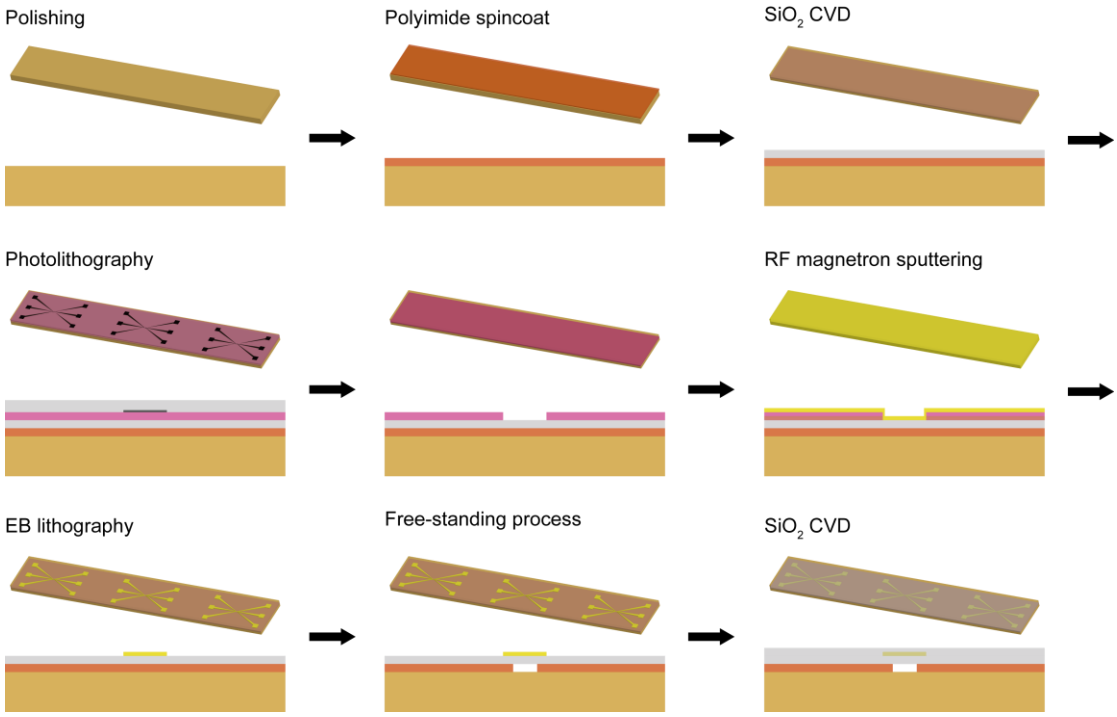

Figure 3.2.2. Fabrication process of insulator protected MCBJ substrate.

3.2.2. Current measurement setup

Formations of molecular sized gaps were performed using the insulator-protected MCBJ (SiO_2-MCBJ) devices in vacuum < 10^{-5}Torr, Milli-Q water, and TE buffer at room temperature. This device was set in a three point bending configuration and bended mechanically from the back by a piezo-driven pushing rod. At the same time, the dc voltage V_b was applied to the junction and the conductance G was measured by a Keithley 6487 picoammeter/source unit. In this experiment, the electrical conductance was used as a parameter for controlling the mechanical deformation of Au junction (The increasing and decreasing of piezo voltage V_p would retract and push the substrate so as to make the electrode gap size smaller and wider, respectively.).[10] Specifically, when $G > 6G_0$ or $G \leqq 6G_0$, junctions were extended at a displacement rate of 1 nm/s or 0.0006 nm/s, respectively ($G_0 = 2e^2/h$ is the conductance quantum). After breaking, junction was closed at a speed 1 nm/s untill G got above $15G_0$; formation and breaking of the contacts were repeated for hundreds of times while recording temporal changes in the junction conductance. These process are carried out using a program code written with Microsoft Visual Basic 6.0 that GPIB-control the Keithley 6487 picoammeter/source and piezo-voltage.

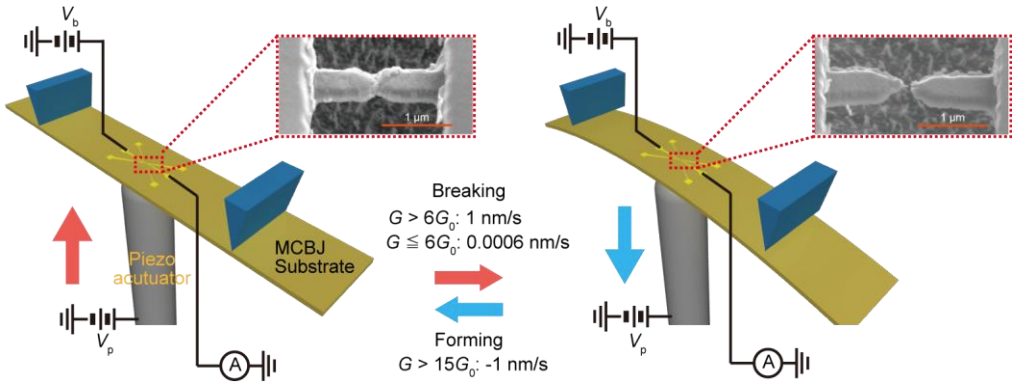

Figure 3.2.3. Gap size control via piezo voltage.

3.2.3. Electrode gap formation using insulator-protected MCBJ devices

For examination of break junction capabilities, tunneling electron transport in vacuum was investigated utilizing insulator-protected MCBJ device. In the gap formation, a junction was first broken through the aforementioned beam bending control (inset of Fig. 3.2.4(a)). After breaking, the thus created electrode gap was widened by about 0.3 nm through decreasing the piezo-voltage V_p by -7 V. Then, the gap was closed gradually by increasing V_p in a stepwise fashion. After that, current I flowing between the electrodes was recorded at every each point of 0.07 V increment of V_p (Fig. 3.2.4(a)). This measurement was continued until I got above 10 nA. Subsequently, the junction was closed to $G > 15\ G_0$. The two-dimensional histogram I against V_p for 200 consecutive traces of the break junction measurements (Fig. 3.2.4(b)) reveals exponential increase of current for over four orders of magnitude with decreasing the inter-electrode distance d_{gap}. This suggests charge transmission through a tunneling barrier in a vacuum gap between the insulator-protected Au nanoelectrodes. In addition, cluster of the plots within the linear band indicates the Au junction underwent hundreds of formation and breaking processes in a highly reproducible manner; although lateral shifts of the curves reflect an atomic-scale variation in the size of electrode gap formed, they do not seem to affect the tunneling current dependence on V_p.[11] For characterization of the tunneling current decay, we assess the slope of linear Log(I)-V dependence. For example, Fig. 3.2.4(c) was seen that whereas the conductance $G = I/V_b$ at $V_b = 0.1$ V is under the detection limit of the picoammeter when the distance between the electrodes is large, it starts to increase exponentially with V_p above 7 V. The relationship of $G \sim e^{\alpha V_p}$ with $\alpha = 1.16$ was obtained by linear fit from 9 V to 15 V. In theory, tunneling conductance dependence on the gap

distance d is written as $G \sim e^{-2\kappa d_{gap}}$, where $\kappa = \sqrt{2m_e\Phi/\hbar^2}$ is the decay constant. Comparing this equation to the experimental value of αV_p, the ratio $R = d_{gap}/V_p$ was acquired in the assuming of the electron mass $m_e = 9.11\times10^{-31}$kg and the tunneling barrier $\Phi = 5$ eV from the work function of bulk gold.[12] Considering that the electromotive motion

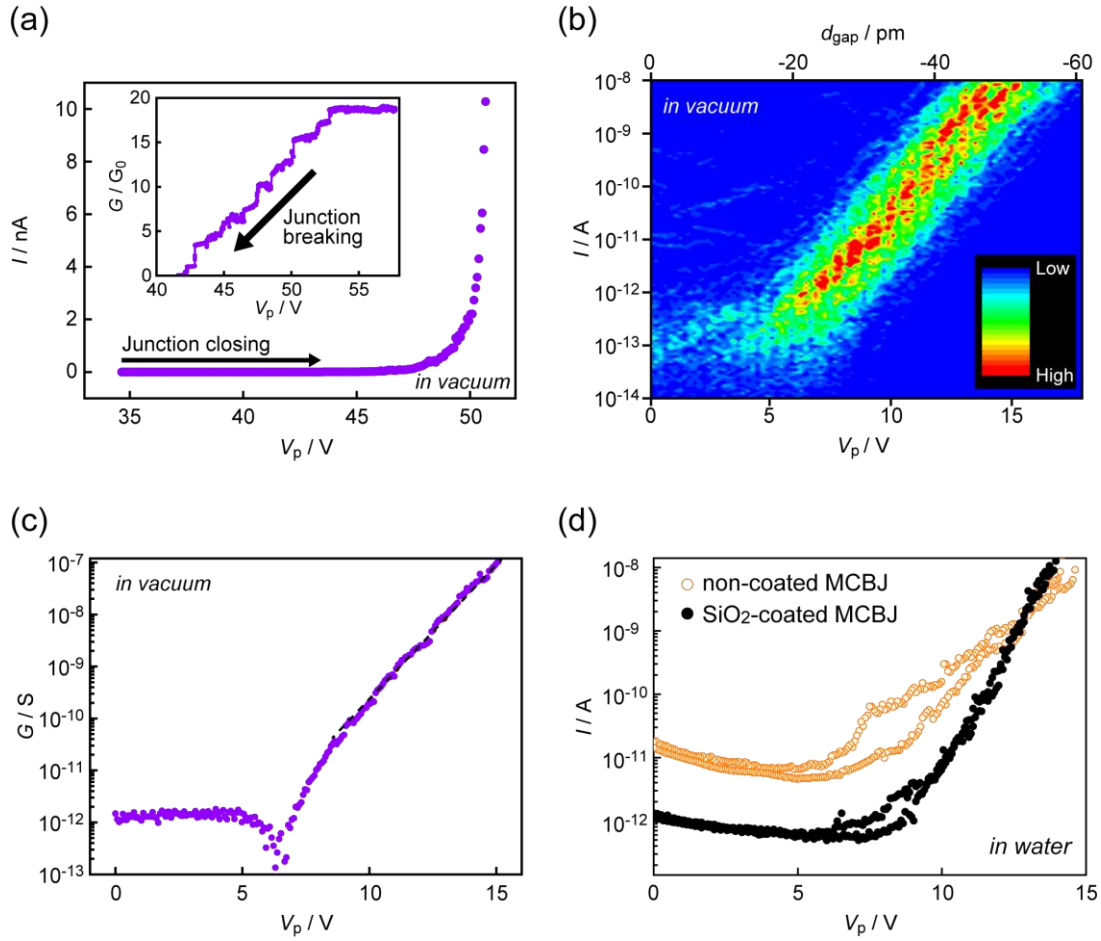

Figure. 3.2.4. (a) Piezo-voltage V_p dependence of current I acquired with a SiO_2-MCBJ in vacuum at room temperature. The electrode gap distance is in proportion to I-V_p. Inset shows the conductance trace during junction breaking. (b) Two-dimensional histogram constructed with I-V_p. (c) Plots of G as a function of V_p. (d) I-V_p curves acquired in Milli-Q using non-coated (orange open circles) and SiO_2-coated MCBJs (black filled circles).

D of the piezo actuator scales as 1 μm/V, the attenuation factor $r = d_{gap}/D = 4.9\times10^{-5}$ is deduced. This value is in close agreement to the analytical expression of $r = 6\xi tu/L^2 = 4.2\times10^{-5}$ with $\xi = 1$, the distance between the supporting points $L = 12$ mm, the substrate

thickness t = 0.5 mm, and the free-standing length of the Au junction u = 2 μm of the MCBJ sample, respectively. Here, ξ is the material coefficient determining the stiffness of substrate, which is about 3 for the soft polyimide layer[13]. Therefore, it seems that covering the polyimide layer by the hard SiO_2 layer decreased ξ to 1. In turn, this result ensure the validity of the barrier height estimated from the work function of Au and the absence of any significant influence of contaminations.[12,14]

The methods described above was applied to investigate the electron tunneling transport in aqueous solution. In the measurement using non-protected MCBJs, I-V_p dependence showed irreproducible manner with large fluctuations in Milli-Q making it difficult to investigate the tunneling decay characteristics (Fig. 3.2.4(d)). Contrastively, insulator protected MCBJs provided well-reproducible I-V_p traces with small current fluctuation. Moreover, the V_p-independent current at the large d_{gap} regime also decreased by an order of magnitude from 10 pA for bare MCBJs to 1 pA. These results are attributable to the suppressed ionic current by the insulator protection of Au electrode surface. Quantitatively, rough estimation of I using the Milli-Q resistivity of 18.2 MΩcm yields 1 pA at V_b= 0.1 V assuming 80 nm square Au parallel plate separated by 3 nm. Consequently, although the actual electrode surface structure at the sensing area is not clear, the constant current flowing through the large electrode gap indicates the conduction through water in the confined space between two electrodes.

Figure 3.2.5(a) shows I- V_p traces measured in vacuum, Milli-Q, and TE buffer (10 mM Tris-HCl, 1 mM EDTA) using insulator-protected MCBJs. In both of the liquid conditions, the rapid increase of the current similar to that in vacuum was observed during gap closure. Before discussing the observed I-V_p dependence, the contact mechanics in the liquid media was considered. The piezo voltage change V_c required to recontact the

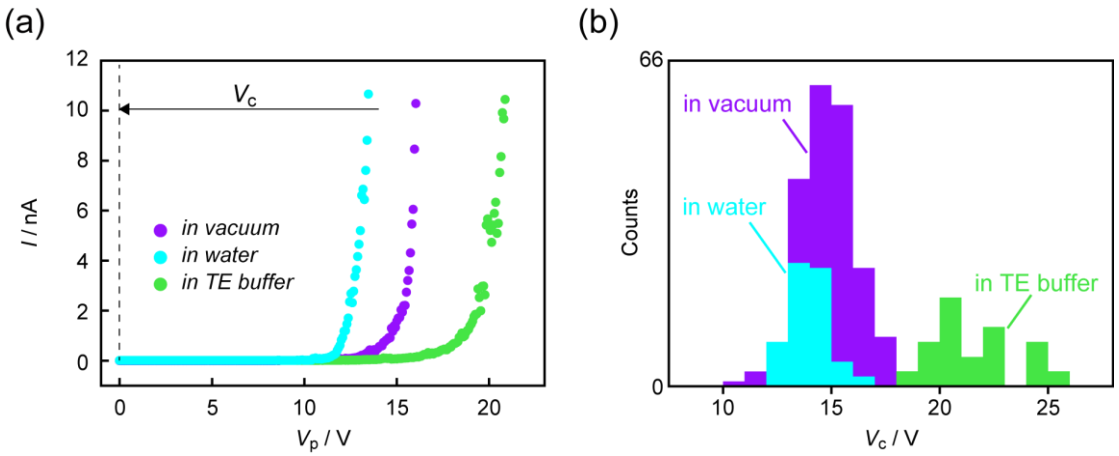

Figure. 3.2.5. (a) Typical I-V_p curves in vacuum (purple), Milli-Q (light blue), and TE buffer (yellow-green). V_c is the piezo-voltage change required to close the junction to $G > 1G_0$. (b) Distributions of V_c. Color coding is the same as that in (a).

broken junction to G above 1 G_0 after the self-breaking was collected (Fig. 3.2.5(a)). In vacuum, typical values of V_c is about 14.8 V (Fig. 3.2.5(b)). Subtracting the initial offset of V_p = 7 V, d_{gap} after self-breaking of the Au contacts was estimated to be 0.72 nm using R in vacuum, which is in good accordance with the previous literatures (the 0.2 nm deviation can be due to a mechanical hysteresis caused by the gap distance expansion after the contact breaking).[10,11] Significantly, the distribution of V_c in water is quite similar to that in vacuum giving d_{gap} = 0.68 nm indicating little influence of the water molecules on the contact mechanics. This result is not surprising considering the large mass difference between Au atoms and H_2O molecules that would give rise to small impact of thermal collisions of water molecules on the contact mechanics.[15,16] In contrast, V_c in TE buffer is larger than the others by about 6 V. As that hydrodynamic pressure plays just a minor role on V_c, it is wondered what has possibly affected the I-V_p characteristics in TE buffer. The gradual extension of the gap distance by electrochemical reaction taking place at the biased gold electrode surface in buffer of pH 8.0 is less probable. In fact, smooth current increase was observed in spite of that tunneling current is highly sensitive to the

electrode gap distance instead of fluctuating I-V_p plot when decreasing the d_{gap}. Therefore, alternatively, it is speculated that the surface reconstruction was modified attributed to the adsorption of electron donating ions on the Au junction surface after the contact breakdown and led to formation of the slightly wider gaps.[17] It is also possible that thermal collision of EDTA molecules (mass density; 292.24 g/mol) comparable to that of

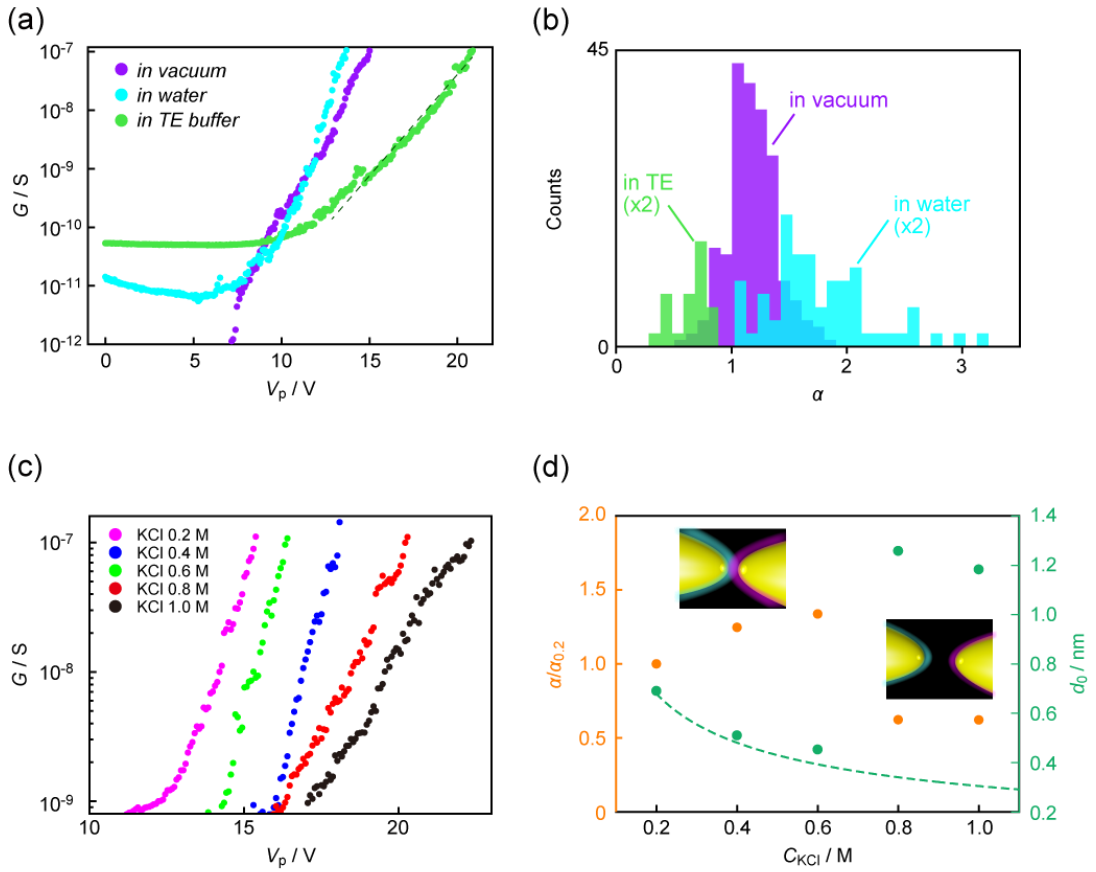

Figure. 3.2.6. (a) Conductance G plotted against V_p. Red, black, and blue circles denote G in vacuum, Milli-Q, and TE buffer. Green dotted line is an exponential fit to the data in TE buffer with $G \sim e^{\alpha V_p}$. (b) Histogram of a constructed with each G-V_p curve measured. Color coding is the same as that in (a). (c) G-V_p curves measured in a salt solution at various KCl concentrations: 0.2 M (pink); 0.4 M (blue); 0.6 M (green); 0.8 M (red); and 1.0 M (black). (d) KCl concentration dependence of the decay constant a normalized by that at 0.2 M, $\alpha_{0.2}$ (orange plots), and the inter-electrode distance at when G = 10^{-7} S (yellow-green plots). Dashed line shows the Debye length.

Au (196.97 g/mol) affect the contact mechanics of the junctions and led to formations of

wider gap.[16]

Now, we compare the decay behavior of tunneling current in different environments. The distance dependence of tunneling conductance from the G-V_p curves measured was deduced. When $d_{gap} > 0.5$ nm, a contact conductance amounts several tens of pA in liquid media. It seems that the distance-independent G is attributed to the ionic current through nanogap between Au electrode surfaces.[18] Except this contribution of ions, the exponential decay, which has different rate with the gap distance, is shown unambiguously in Figure. 3.2.6(a). Interestingly, the slope of decay α for Milli-Q is steeper (Fig. 3.2.6(b)). This can be due to either a higher displacement rate or an enhanced tunneling barrier height than those in vacuum. Nevertheless, the former case seems unlikely from the discrepancies in R in vacuum and Mill-Q $R_{Milli\text{-}Q}/R_{vac}$ estimated from α with $\Phi = 5$ eV. That is to say, there is no influence of H_2O molecules on the tunneling barrier height, which is much larger than $R_{Milli\text{-}Q}/R_{vac} = 1.1$ calculated from the difference in V_c (This situation is similar with that of in TE buffer where $R_{TE}/R_{vac} = 0.2$ was found from α with the bulk Au work function, that is factor of 2.5 smaller than the ratio educed from V_c). Rather, the larger decay constant seems to be suggesting a role of the liquid molecules on the tunneling barrier; having dipole, interaction between H_2O and Au surface would alter the barrier height for electron tunneling in a complicated manner as the overall effect depend on the local structure of water molecule in the electrode gap.[19-21] This also can explain the relatively broad distribution of the decay constant in Milli-Q (Fig. 3.2.6(b)) that would reflect a variation of water molecule structures in the nanospace between Au electrode surfaces. Therefore, the faster decay of tunneling current in Milli-Q indicates that H_2O molecules adsorbs on Au electrode surfaces with the dipole oriented in a direction hindering electron tunneling under the applied voltage as reverse effects

would entail energetically unfavorable molecular conformations involving dissociation of hydrogen bond.[22] On contrary, the conductance decay is slower in TE buffer (Fig. 3.2.6(b)). The positive effect of electrolyte suggests electron tunneling through multiple intermediate states derived from Coulomb interaction between the electrons and ions.[17, 23]

To study the role of electrolyte, the tunneling current measurements extended to TE buffer containing KCl with concentration C_{KCl} from 0.2 M to 1.0 M were conducted. Despite current shows unstable feature in salt solution, the G-V_p semilog plots displayed a feature indicative of charge tunneling through the electrode gaps (Fig. 3.2.6(d)). However, the decay constant behaved in an intriguing manner; that is, the Log(G)-V_p slope α decreased with increasing the KCl with concentration from 0.2 M to 0.6 M, but it suddenly become low at higher amount condition (plot in Fig. 3.2.6(d)). On the other hand, it should be noted that Debye length λ tends to be shorter with concentration of KCl (dashed curve in Fig. 3.2.6(d)).[24] When the gap size is compared with λ, the inter-electrode distance d_0 at $G = 10^{-7}$S estimated by extrapolating the exponential dependence to $G = 1G_0$, is smaller or larger than 2λ for $C_{KCl} \leq 0.6$ M or $C_{KCl} \geq 0.8$ M, respectively (blue plot in Fig. 3.2.6(d)). Thus, at the point where $G = 10^{-7}$S, the electrical double layer of the electrode surface is merged or separated in each case. When these layers are overlapped, the screening becomes inefficient and charge distribution in the electrode gap would tend to be more irregular. This is expected for the transition in α since the local ion arrangement in vicinity of the electrode surface would noticeably affect tunneling probability.

In this section, we have showed that insulator-protected MCBJ device can be a reliable tool to investigate quantum transport in aqueous solutions. Moreover, the

reproducible tunneling conductance curves are useful for calibrating the accurate electrode size from the current state in electrolyte solutions. These character would enable to improve the sensing capability in single-biomolecule with the MCBJ technique via providing fine-adjustment of the electrode gap size to the target analyte in an electrolyte conditions and the ionic background current suppression for the identification of molecule by tunneling current with better accuracy.

Reference of this section

1. N. J. Tao, *Nat. Nanotechnol*. **1**, 173 (2006).
2. S. M. Lindsay and M. A. Ratner, *Adv. Mater*. **19**, 23 (2007).
3. H. Song, M. Reed, and T. Lee, *Adv. Mater*. **23**, 1583 (2011).
4. N. A. Zimbovskaya and M. R. Pederson, *Phys. Rep*. **509**, 1 (2011).
5. M. Tsutsui and M. Taniguchi, *Sensors* **12**, 7259 (2012).
6. B. Xu and N. J. Tao, *Science* **301**, 1221 (2003).
7. M. Tsutsui, M. Taniguchi, K. Yokota, and T. Kawai, *Nat. Nanotechnol*. **5**, 286 (2010).
8. M. Tsutsui, K. Matsubara, T. Ohshiro, M. Furuhashi, M. Taniguchi, and T. Kawai, *J. Am. Chem. Soc*. **133**, 9124 (2011).
9. M. Krems, M. Zwolak, Y. V. Pershin, and M. Di Ventra, *Biophys. J.* **97**, 1990 (2009).
10. M. Tsutsui, K. Shoji, M. Taniguchi, and T. Kawai, *Nano Lett*. **8**, 345 (2008).
11. M. Tsutsui, M. Taniguchi, and T. Kawai, *Appl. Phys. Lett.* **93**, 163115 (2008).
12. Y. Yamada, A. Sinsarp, M. Sakaki, and S. Yamamoto, *Jpn. J. Appl. Phys.* **42**, 4898 (2003).
13. S. A. G. Vrouwe, E. van der Giessen, S. J. van der Molen, D. Dulic, M. L. Trouwborst, and B. J. van Wees, *Phys. Rev. B* **71**, 035313 (2005).
14. A. Vaught, T. W. Jing, and S. M. Lindsay, *Chem. Phys. Lett.* **236**, 306 (1995).
15. Q. Pu, Y. Leng, X. Zhao, and P. T. Cummings, *Nanotechnology* **18**, 424007 (2007).
16. M. Tsutsui and M. Taniguchi, *J. Appl. Phys.* **113**, 024303 (2013).
17. W. Schmickler, *Chem. Rev*. **96**, 3177 (1996).
18. G. E. Kimball, *J. Chem. Phys.* **8**, 199 (1940).
19. D.-H. Woo, E.-M. Choi, Y.-H. Yoon, J.-J. Kim, I. C. Jeon, and H. Kang, *Surf. Sci*. **601**, 1554 (2007).

20. C. S. Cucinotta, I. Rungger, and S. Sanvito, *J. Phys. Chem. C* **116**, 22129 (2012).

21. P. Boynton and M. Di Ventra, *Phys. Rev. Lett*. **111**, 216804 (2013).

22. W. Schmickler, *Surf. Sci.* **335**, 416 (1995).

23. S. Boussaad, B. Q. Xu, L. A. Nagahara, I. Amlani, W. Schmickler, R. Tsui, and N. J. Tao, *J. Chem. Phys.* **118**, 8891 (2003).

24. J. Israelachvili, *Intermolecular and Surface Forces*, 2nd ed. (Academic Press, London, 2003).

3.3. Protein discrimination by insulator-protected MCBJ devices

Roles of proteins are one of the fundamental point for life activities. Their utilities are often linked to their conformation and electrical property directly. As described in the general introduction, countless attempt were conducted to realize their feature. For instance, recently, the research about development of super-resolved fluorescent microscopy deserved novel prize in chemistry 2014.[1-3] This research enables to approach to cell and biomolecule observation with single-microscale order. Through, in general, the scales of biomolecules which works sorely are usually nano-micro meter order and such observations need fluorescent modification. Thus for further analysis, different types of method which provide modification free and nanoscale analysis is needed.

The analysis for such features in single molecule range would provide wealthy understanding in the adequate scale about their work. Until now, these characters have been analyzed using scanning tunneling microscopy,[4] conductive atomic force microscopy,[5] and so on. The conductive feature of proteins are dependent on their region. Various *I-V* curves are thus obtained from a single protein. In addition, many of the experiments were conducted in vacuum conditions. These problems has made it difficult to understanding of charge transport through single-proteins. Recently, an *in situ* STM measurement has gathered attention on the view of quasi-biological environment.[6] Nevertheless, even such a measurement, the target analytes must be fixed on the substrates in a form of a self-assembled monolayer formed on substrate for instance. Such restriction would prohibit comprehensive interpretation in actual conditions they work

wherein proteins are free to change the conformations and interact with other chemical species.

In this section, the protein discrimination was conducted using an insulator-protected MCBJ device to measure the single-molecule conductance. This measurement was implemented in liquid condition without any modification to target proteins. These measurement conditions enable evaluation of the electrical conductivity of analytes, the trace of which is expected to provide the information of protein conformations in the electrode gap at the single-molecule level.

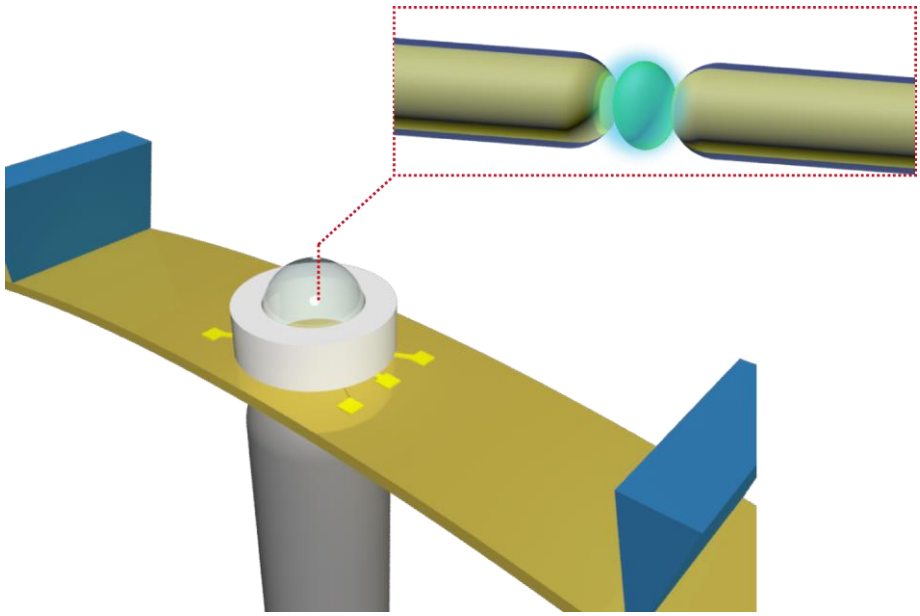

Figure 3.4.2. Single molecule measurement in liquid conditions using nanoelectrodes.

3.3.1. The evaluation of protein conductivity in liquid conditions

The fabrication process of the MCBJ device and measurement setup were shown in Figure 3.2.1 and 3.2.2. In this measurement, the gap distance between the electrodes was kept constant via the piezo voltage control. For the present MCBJ set up giving the displacement ratio of the order of 10^{-5}, the fluctuations of the gap distance acquired from piezo voltage are estimated to be negligible. In this section, the two proteins, cytochrome *c* (cyt *c*; 2.5×2.5×3.7 nm^3)[7] and bovine serum albumin (BSA; 14×4.0×4.0 nm^3)[8] were utilized as target molecules (Figure 3.2.2). They have largely different length-to-diameter aspect-ratio structure. The measurements were conducted with the condition of applied voltage V_b= 0.5 V, concentrations of each protein $C = 1.0 \times 10^{-4}$M in PBS buffer (13.70 mM NaCl, 0.81 mM Na_2HPO_4, 0.268 mM KCl, 0.147 mM KH_2PO_4).

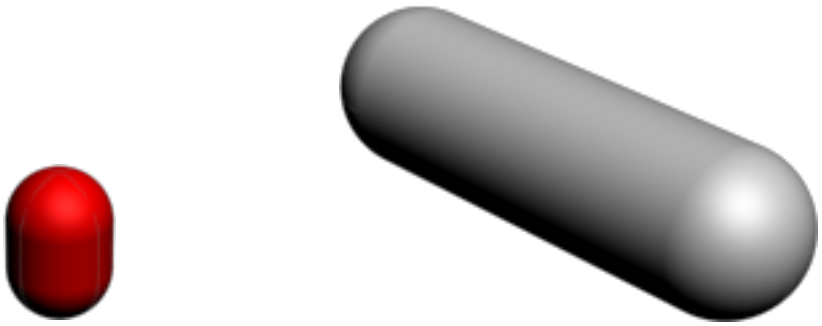

Figure 3.4.2. The conformation of proteins (cyt *c*; red and BSA; gray) represented in capsule forms. Both images are in same scale.

There are two possible changes in the inter-electrode current upon trapping single-proteins in the electrode gap; the suppression of ionic current and enhancement of tunneling current. In the former case, incursion of analyte to a nanoscale gap interfere the ion transport between the dc-biased electrodes via the volume exclusion effect. In another case, the proteins electrically couple to the electrodes and thereby offer conduction

channels for charge transmission via the frontier molecular orbitals, which would give rise to current enhancement. In actual measurements, both the effects can appear simultaneously to cause a change in the current during single-molecule trapping.

For adjusting the gap size to the size of molecules, a calibration was conducted (Figure 3.4.3). After the breaking of junction, the gap distance was expanded to some extent and then contracted until $I > 10^{-8}$ A. In this process, the difference of V_{piezo}, ΔV_0, was acquired using the slope of linear fitting β about current decay and the substrate was pushed further via arbitral setting of V_{piezo}. In the measurement, the V_{piezo} was kept constant to maintain the gap distance unchanged. After the measurement, the mode value of V_{piezo}, V_{end}, was obtained and the second difference between $I = 10^{-8}$ A to the setting point, ΔV_2, was also acquired. Under the two assumptions of 1) the definition of an Au monatomic chain formation at $d_{gap}= 0$ and 2) the exponential decrease of tunneling current, utilizing these two ΔV, the gap distance is derived via the equation $d_{gap}= \alpha(\Delta V_0+\Delta V_1)$ where α is the product of the device parameter 4.2×10^{-5} and displacement of piezo actuator 1×10^{-6} V^{-1}. This calibration would provide adequate estimation for gap distance.

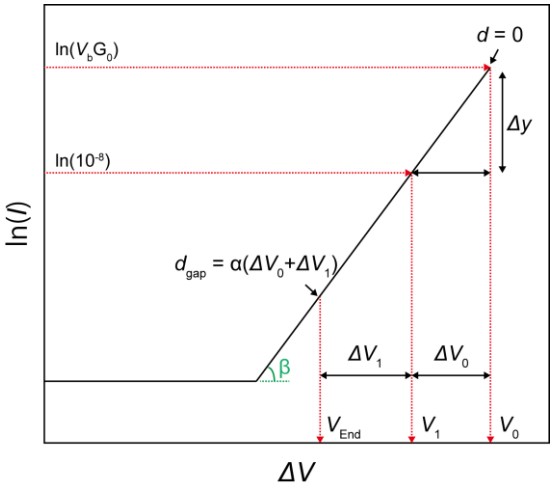

Figure 3.4.3. The values required in the calibration in the graph of exponential current decreasing.

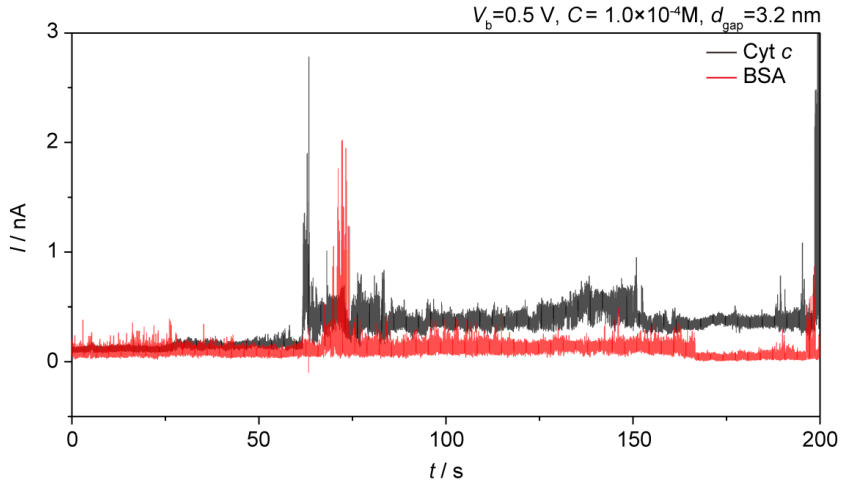

Figure 3.4.4. The long-term current traces of both proteins.

The typical long-term current traces is shown in Figure 3.4.4. The every current trace including these traces, the current decreasing from the offset value which might indicate the decreasing ionic current by volume exclusion effect of proteins cannot be found and the conductance histograms were constructed using these traces and V_b. In Figure 3.4.5, the shift of conductance with the expanding gap size is shown. In the narrow gap, the various peaks were observed. However, with widening, such peaks are disappeared and re-appeared in gap expanded further. Possible reasons of this change is due to restriction of the molecular conformations in the sub-molecule sized electrode gaps. W. Haiss[9] and his colleagues focused on the conductance dependence of tilt angles for

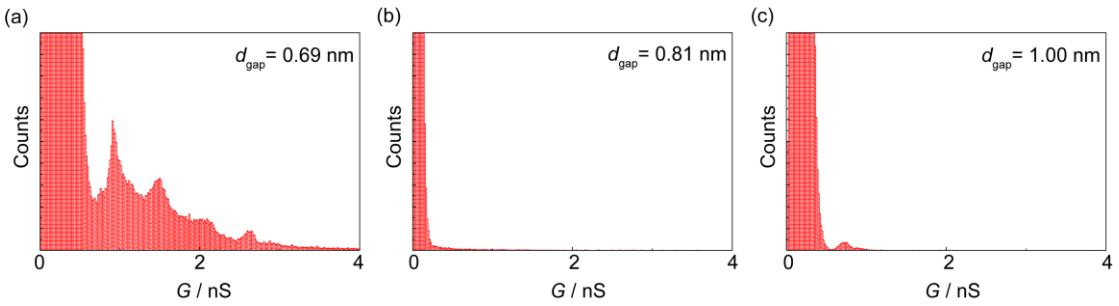

Figure 3.4.4. The gap distance dependence of conductance of cytochrome *c*.

some organic compounds theoretically. The expanding gap distance might also regulate the orientations of molecules and determined various conductance.

Furthermore, the concentration dependence of the current traces is shown in Figure 3.4.6(a-c). For ease of instinctive understanding about measurement situation,

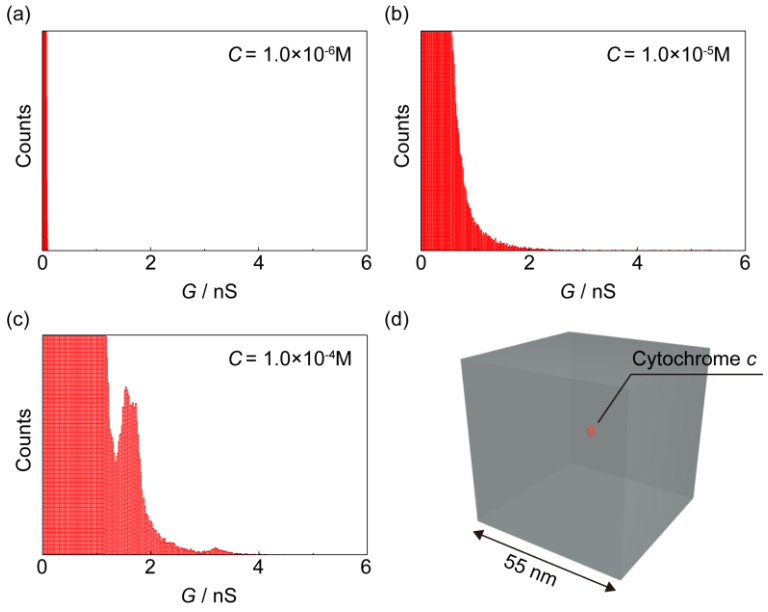

Figure 3.4.6. The concentration dependence of conductance of cytochrome *c* (a-c) and the graphical image of volume occupied by single cytochrome c molecule for 1.0×10^{-5}M solution.

figure 3.4.6(d) shows the solution volume occupied by the single molecule at $C = 1.0\times10^{-5}$ M solution. With the increasing of concentration, the conductance started to show ups and downs indicating molecular trap between the electrodes whereas there is no obvious change in the conductance at the low concentrations due to the little chance for the proteins to come across the sensing zone by diffusion. Therefore, the molecular concentration of 1.0×10^{-4} M was selected in the next comparison measurement.

Figure 3.4.7 is the representative current traces about two proteins, BSA and cyt. *c*. In both traces, the sudden increase and decrease in the current might be attributed to adventitious incursion to and escape from the electrode gap. The conductance histograms constructed by current traces is shown in Figure 3.4.8. In the histogram of cyt *c*, there are multiple peaks and some of the peaks are found at integral multiples of a certain conductance value G_{cyt} = 0.72 nS. In the field of single molecule electron transport studies, this characteristic relationship is accepted as reflecting the number of molecules bridged between the nanogap in parallel. Considering the size scales of cyt *c* and the width of nanogap, which is set to 3.2 nm, together with the thiol anchoring group in the protein molecule, such Au-molecule contact formation is conceivable. The other possible reason explaining the stepwise increase in the current are the self-assembly of cyt *c* on Au.[10] To shed light on this discriminations, the comparison of contact condition is needed

To explore further information on the protein, the fluctuations in the conductance were investigated. It was found that the width of each peak in the histogram becomes broader with increasing conductance. These widths reflect the magnitude of temporal conductance fluctuations associated with changes in the molecular orientations. Therefore

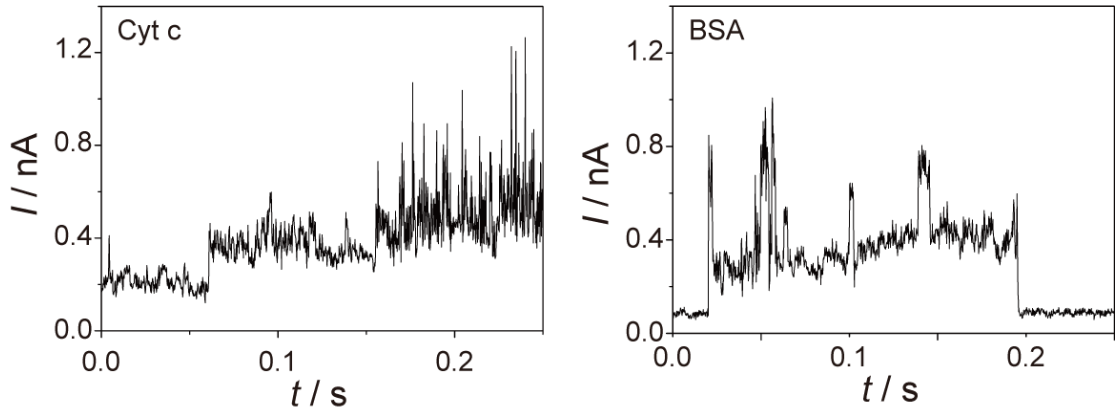

Figure 3.4.7. The representative current trace of both proteins.

this difference is reasonable because increase in the number of molecules bridging the electrodes indicates more scatterers to cause larger conductance fluctuations.

On the other hand, in the distribution of BSA, only two peaks were observed in the histogram with the 3.2 nm gap distance; quite different from the one obtained for cyt *c*. Considering the high aspect ratio structure, the behaviors of the conductance when BSA molecule enters the nanogap were affected more drastically by their conformation than cyt *c*, which has a spherical shape. Therefore this type of conductance is also concerning the report of W. Haiss[9] described above and high conformational aspect provides various

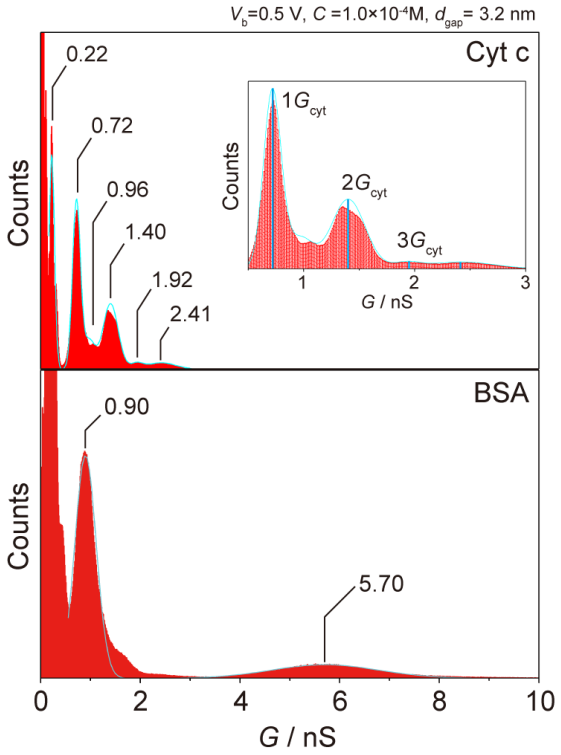

Figure 3.4.8. Conductance histograms of cytochrome c and bovine serum albumin.

conductance. However, it is interesting that the value of first conductance peak is larger than the ones obtained for cyt. *c*. Therefore there is another possibility of occurring more path for electron transfer by making more contact with electrode.

The conductance fluctuations were studied in more detail by examining noise analysis. O. Adak and his colleagues[11] reported the correlation between the current noise and the variations in the contact motif between molecules and metallic electrode surface. In this report, the noise acquired from the conductance measurements of single-organic molecules was focused. The noise spectra revealed characteristic slope close to -1 depending on the molecules measured. The difference was attributed to the metal-molecule linkage where the molecules are bonded to the Au electrodes through Au-amine bonds or weak coupling through space without any chemical bond formations. Thus this analysis was adopted to the present case. After the collection and joint of current values between 95 % confidence interval, which constructs about 95% of each histogram under the assumption of normal distribution, Fourier transfer was adopted to these current trace. The result is shown in Figure 3.4.9. As in the figure, all the spectra have no clear sloping feature. In general the noise, which has no relationship with its frequency is thermal noise. The report of O. Adak[11] introduced above first showed that the flicker noise of single molecule junctions are originated from changes in the molecular coupling attributed from electrode atom switching between metastable configurations at room temperature. Considering the effect of thermal collision to the electrode surface revealed in section 3.2.2 has enough effect to destabilize the Au electrode surface, the noise tendency in this measurement could be possible since the switching process are disturbed. However, their noise amplitude might show conductance dependence and the slopes about higher conductance has little value. Therefore, the combination of the differences of amplitude and gradient might useful for assignment between conductance and contact.

In this section, as conclusion, conductive evaluations were conducted about two type proteins using insulator protected MCBJ devices developed in the research of section

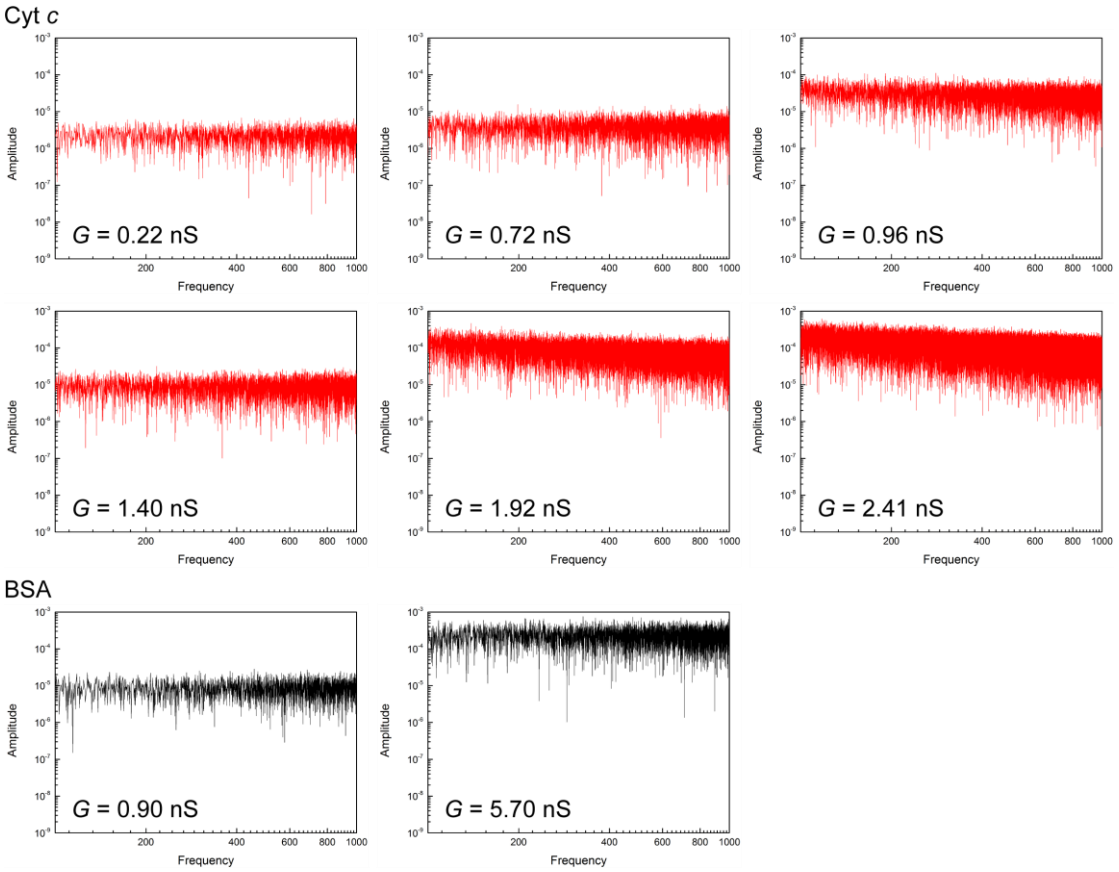

Figure 3.4.9. The FFT results of each conductance peaks of both proteins

3.2. The effect of ionic decreasing could not observed and tunneling current are dominated. The conductive distribution shows obvious difference between proteins. Such difference are useful for the discrimination in quasi-biological environment. However, the problems of stepwise increasing and the origin of other peak which does not show integral multiple relationship are left, therefore, the combination of other measurement technique such as nanopore trapping method is needed for further analysis.

Reference of this section

1. E. Betzig, G. H. Patterson, R. Sougrat, O. W. Lindwasser, S. Olenych, J. S. Bonifacino, M. W. Davidson, J. Lippincott-Schwartz, H. F. Hess, *Science* **313**, 1642 (2006)
2. T. A. Klar, S. Jakobs, M. Dyba, A. Egner, S. W. Hell, *Proc. Natl. Acad. Sci. USA* **97**, 8206 (2000)
3. R. M. Dickson, A. B. Cubitt, R. Y. Tsien, W. E. Moerner, *Nature* **388**, 355 (1997)
4. E. A. Della Pia, Q. Chi, D. D. Jones, J. E. Macdonald, J. Ulstrup, and M. Elliot, *Nano Lett.* **11**, 176 (2011)
5. D. Xu, G.D. Watt, J. N. Harb, and R. C. Davis, *Nano Lett.* **5**, 571 (2005)
6. Q. Chi, O. Farver, and J. Ulstrup, *Proc. Natl. Acad. Sci. USA* **102**, 16203 (2005)
7. A. K. Wright, M. R. Thompson, *Biophys. J.* **15**, 137 (1975)
8. I. Ichinose, R. Takaki, K. Kurokawa, and T. Kunitake, *Langmuir* **19**, 3883 (2003)
9. W. Haiss, C. Wang, R. Jitchati, I. Grace, S. Martin, A. S. Batsanov, S. J. Higgins, M. R. Bryce, C. J. Lambert, P. S. Jensen and R. J. Nichols, *J. Phys.: Condens. Matter* **20**, 374119 (2008)
10. S. Chah, C. V. Kumar, M. R. Hammond, and R. N. Zare, *Anal. Chem.* **76**, 2112 (2004)
11. O. Adak, E. Rosenthal, J. Meisner, E. F. Andrade, A. N. Pasupathy, C. Nuckolls, M. S. Hybertsen, and L. Venkataraman, *Nano Lett.* **15**, 4143 (2015)

Chapter 4 Conclusions and remarks

In this thesis, electrical analysis of single-molecule and –particle using extended-nanospace; nanopores and nanoelectrodes were conducted experimentally. The new findings in this study is summarized as follows.

In chapter 2.2, electrical detections of single-particles were performed by a resistive pulse method using an ultra-low thickness-to-diameter-aspect-ratio synthetic nanopore. Ionic current signal heights smaller than theoretical values considering only ion exclusion effects, which was attributed to contributions of particle surface charges to increase the ion density in the pore during the translocation. Electrophoretic translocation of equi-sized nanoparticles yielded ionic current signatures distinct to the particle surface modifications, thereby demonstrating particle discrimination not but the size but by the surface charge density.

In chapter 2.3, the voltage-specific target capture via surface charge density was conducted by nanopore trapping method. The floating condition of particles in trapping was confirmed by the tendency of voltage dependence to amplitude of ionic-flow suppression. Besides, the possibility of controlling particle position of z-direction was shown via modulation of bias voltage. The discrimination of different-sized particles was demonstrated by the comparison between fractions of ionic current blockade about mixture and solitary particle conditions.

In chapter 2.4, simultaneous measurements of fluorescence and the cross-pore ionic current was performed for studying single-particle trapping mechanism in a synthetic low thickness-to diameter aspect ratio nanopore. Voltage-controlled trapping and detrapping of single-nanoparticles were confirmed by the fluorescent images and the

ionic current blockage. Trapped particles are being floated from the pore by several tens of nanometer due to the cationic electroosmotic flow in the SiN nanopore. Balance between the electrophoretic and electroosmotic drag forces determines the nanoscale position of nanoparticles electrically trapped at nanopore orifice. Brownian motions cause little influence on the position of trapped particles.

In chapter 3.2, SiO_2-coated mechanically-controllable break junctions (SiO_2-MCBJs) was developed that can form a pair of dielectric-protected Au nanoprobes with nanometer separation. SiO_2-MCBJs can suppress the ion contributions to the net current flow and allow reproducible measurements of tunneling conductance decay with distance in an aqueous solution. Tunneling barrier height increases when electric double layers on the current sensing electrodes merge together.

In chapter 3.3, the discrimination of proteins via evaluation of protein conductivity in liquid condition was conducted. In situ conductive evaluation without immobilization of analyte was achieved and this research must helpful for adequate investigation of biomolecules.

The author developed single-molecular and –particle analysis using nanopore and nanoelectrodes. In addition, the author shows the combination of these factors has possibility to become one of the ideal analytical method for single-molecular and –particle analysis via this doctoral dissertation.

List of publications

"Discrimination of equi-sized nanoparticles by surface charge density using low-aspect ratio nanopore"

A. Arima, M. Tsutsui, and M. Taniguchi

Applied Physics Letter **104**, 163112 (2014)

"Fabrications of insulator-protected nanometer-sized electrode gaps"

A. Arima, M. Tsutsui, T. Morikawa, K, Yokota, and M. Taniguchi

Journal of Applied Physics **115**, 114310 (2014)

"Electrical trapping mechanism of single-microparticles in a pore sensor"

A. Arima, M. Tsutsui, Y. He, S. Ryuzaki, and M. Taniguchi

AIP Advance **6**, 115004 (2016)

"Volume discrimination of nanoparticles via electrical trapping using nanopores"

A. Arima, M. Tsutsui, and M. Taniguchi

Journal of Nanobiotechnology **17**, 40 (2019)

"Thermoelectric Voltage Measurements of Atomic and Molecular Wires Using Microheater-Embedded Mechanically-Controllable Break Junctions"

T. Morikawa, A. Arima, M. Tsutsui, and M. Taniguchi

Nanoscale **6**, 8235 (2014)

"Thermoelectricity in atom-sized junctions at room temperature"

M. Tsutsui, T. Morikawa, A. Arima, and M. Taniguchi

Scientific Reports **3**, 3326 (2013)

"High thermopower of mechanically stretched single-molecule junctions"

M. Tsutsui, T. Morikawa, Y. He, A. Arima, and M. Taniguchi

Scientific Reports **5**, 11519 (2015)

"Particle Trajectory Dependent Ionic Current Blockade in Low-Aspect-Ratio Pores"

M. Tsutsui, Y. He, K. Yokota, A. Arima, S. Hongo, M. Taniguchi, T. Washio and T. Kawai

ACS Nano **20**, 803 (2016)

"Rapid structural analysis of nanomaterials in aqueous solutions"

S. Ryuzaki, M. Tsutsui, Y. He, K. Yokota, A. Arima, T. Morikawa, M. Taniguchi, and T. Kawai

Nanotechnology, **28**, 155501 (2017)

Acknowledgements

This study was carried out at The Institute of Scientific and Industrial Research (ISIR), Department of Chemistry, Graduate School of Science, Osaka University from 2013 to 2016. This work was supported by Grant-in-Aid for JSPS Fellows Grant Number 15J05282.

Foremost, I would like to express my sincere gratitude to Professor Masateru Taniguchi, ISIR, Osaka Univ., for stimulating discussions, continuous encouragement, and providing me the precious opportunity of study in his laboratory.

I also owe a very important debt to Professor Yasuhiro Nakazawa and Professor Takuya Matsumoto, Department of Chemistry, Graduate School of Science, Osaka Univ., for their crucial and fruitful comments on this thesis.

In addition, I profoundly acknowledge Associate Professor Makusu Tsutsui, ISIR, Osaka Univ., for his pleasant guidance and provision of fulfilling life in my Ph. D. course.

Besides, I am indebted to Assistant Professor Hiroyuki Tanaka, and Kazumichi Yokota, ISIR, Osaka Univ., for providing me kind advice and pleasant conversation for research and daily life.

Furthermore, I would like to show my special thanks to everyone who support me, especially the laboratory members for their moral support and warm encouragements. Without them, this work would not have been successful.

Lastly, I would love to express the deepest appreciation to my family for the psychological and financial support, and understanding of my study. I dedicate this thesis to them.

Akihide Arima